

Microlayer formation and depletion beneath growing steam bubbles

Susann Hänsch*, Simon Walker

Imperial College London, Exhibition Road, London SW7 2AZ, United Kingdom



ARTICLE INFO

Article history:

Received 10 July 2018

Revised 21 October 2018

Accepted 20 November 2018

Available online 1 December 2018

Keywords:

Nucleate boiling

Microlayer formation

Microlayer evaporation

Bubble growth

Interface-tracking

Evaporative thermal resistance

ABSTRACT

Microlayers, the few-microns-thick layers of liquid that sometimes remain beneath bubbles growing on a heated substrate, are widely observed in experiments, but theoretical understanding of their formation, behaviour and role in bubble growth is limited.

In this paper we present detailed interface-tracking simulations of the formation and depletion of such microlayers. Validation of our results is presented to the degree that available measurements of such a rapid and microscopic phenomenon allow.

The work extends previous mechanistic hydrodynamic-only CFD simulations of early microlayer formation up to typical bubble departure times. These calculations confirm the understanding that the bubble growth rate and the resulting bubble shape determine the presence and overall extent of microlayers underneath steam bubbles. Their thickness is strongly influenced by viscous effects and surface tension.

We then present coupled, physically self-consistent CFD simulations of the formation and evaporative depletion of such microlayers. This modelling suggests strongly that the evaporation process itself constitutes a significant fraction of the small resistance to heat and mass transfer presented by the very thin liquid layer. Inclusion of representations of evaporative thermal resistance, consistent with those suggested in the literature, is seen to promote the prediction of microlayer formation. Identification of the classes of conditions under which microlayers seem likely to be formed is presented, along with an assessment of their relative contributions to bubble growth. Comparisons of the predictions with recent detailed microlayer measurements indicate good agreement.

© 2018 Elsevier Ltd. All rights reserved.

1. Introduction

One of the processes involved in the growth and departure of steam bubbles from heated surfaces is the formation and evaporation of liquid microlayers. These thin layers of only a few microns thick are formed when an expanding bubble leaves behind liquid between the wall and the underside of the bubble during the early stages of bubble growth. Being all that separates the superheated solid surface from the saturated vapour within the bubble, microlayers evaporate rapidly, thereby causing rapid bubble growth, and in turn further microlayer formation. Via these coupled processes microlayers can play a significant role in bubble growth.

Continued attempts to achieve greater fidelity in modelling of boiling have led to much study of microlayers and their evaporation. This covers both component-scale treatments of wall boiling CFD, in the framework of the RPI model (Gilman and Baglietto, 2013; Colombo and Fairweather, 2015), and micro-scale simulations of single bubbles, where the gas-liquid interfaces are re-

solved via interface-tracking (Sato and Ničeno, 2015; Chen and Utaka, 2015). In both cases the models of microlayer evaporation used, however, are semi-empirical, based on the limited experimental data available.

This paper attempts to investigate mechanistically the formation and self-consistent evaporative depletion of a microlayer during the early stages of bubble growth. By resolving the fluid mechanics of a liquid film being formed underneath an expanding bubble, and coupling this with analysis of its depletion, via a mechanistic evaporation model that incorporates solving for the transient heat conduction in the solid underneath, we aim to add to the understanding of the mechanisms involved in the microlayer formation and evaporation.

In Section 2 we present a review of the experimental observations of microlayers, illustrate the microlayer profiles typically measured underneath steam bubbles at atmospheric pressure and discuss the role microlayers are believed to play in determining bubble growth. We then present the various published works on analytical and empirical modelling of microlayer formation.

In Section 3 the modelling approach adopted in this paper is described.

* Corresponding author.

E-mail addresses: s.haensch13@imperial.ac.uk, s.haensch@imperial.ac.uk (S. Hänsch).

Nomenclature

Roman symbols

a	Accommodation coefficient
c_{pl}	Specific heat capacity of the liquid $J\text{kg}^{-1}\text{K}^{-1}$
C	Constant of initial microlayer thickness
f	Body force vector Nm^{-3}
h_{fg}	Latent heat of evaporation Jkg^{-1}
h_{lv}	Evaporative heat transfer coefficient $\text{Wm}^{-2}\text{K}^{-1}$
H	Heaviside step function
$\dot{m}_{\text{Bubble}}''$	Vapour evolution rate from the curved surface $\text{kgm}^{-2}\text{s}^{-1}$
\dot{m}_{ML}''	Vapour evolution rate from the microlayer $\text{kgm}^{-2}\text{s}^{-1}$
n	Unit vector normal to the interface
p	Pressure Nm^{-2}
$r_{\text{base}}, r_{\text{dry}}$	Bubble base radius, dry-out radius m
u	Velocity vector ms^{-1}
R_{Gas}	Gas constant $\text{Jkg}^{-1}\text{K}^{-1}$
t	Time s
T_{sat}, T_w, T_i	Saturation temperature, wall temperature, interface temperature K

Greek symbols

α_l	Liquid thermal diffusivity m^2s^{-1}
β	Scriven growth parameter
δ	Thickness m
$\delta_0, \delta_{0, \text{hd}}$	Initial thickness, hydrodynamic thickness m
δ_l	Interface Dirac delta function
ϕ	Level set function m
κ	Curvature m^{-1}
λ_l	Liquid thermal conductivity $\text{Wm}^{-1}\text{K}^{-1}$
μ	Dynamic viscosity $\text{kgm}^{-1}\text{s}^{-1}$
$\theta_{\text{app}}, \theta_{\text{triple line}}$	Apparent contact angle, triple line contact angle $^\circ$
ρ_v, ρ_l	Vapour density, liquid density kgm^{-3}
ν_l	Liquid kinematic viscosity m^2s^{-1}
σ	Surface tension coefficient Nm^{-1}

Non-dimensional groups

Ja	Jakob number $\frac{\rho_l c_{pl}(T - T_{\text{sat}})}{\rho_v h_{fg}}$
----	--

Section 4 then presents an extensive validation of our results to the degree present measurements allow. A validation is done both for the hydrodynamic-only results and the results including the evaporation from and depletion of the microlayer.

General predictions of the microlayer behaviour are then given in Section 5. We present predictions of the hydrodynamic-only formation of microlayers underneath growing steam bubbles, and then extend this to present predictions of their formation accompanied by their simultaneous, physically self-consistent depletion. We investigate the significance of the bubble growth rate and the effect of the evaporative thermal resistance during the microlayer formation and evaporation process.

Conclusions and suggestions as to where future work would be fruitful are given in Section 6.

2. Background

2.1. Microlayer terminology

The term ‘microlayer’ refers to the very thin films of liquid that are left behind at the wall underneath the base of rapidly growing vapour bubbles. A sketch of the underside of a ‘typical’ steam

bubble under atmospheric pressure is illustrated in Fig. 1. The microlayer is bound by an inner triple line, where liquid, vapour and solid touch, and an outer ‘apparent’ contact angle, which is typically observed in experiments. The characteristic measured radial extent of the microlayer is about 1 mm, with maximum thicknesses between 1–5 μm. Being all that separates the vapour from the superheated wall this thin liquid film evaporates very rapidly. Microlayers are usually only observed during the early stages of bubble growth and are evaporated within perhaps ~10 ms; generally before the bubble reaches its departure size and leaves the wall.

In order to understand the various experiments and their reporting of microlayer thicknesses it is useful to give a summary of the terminology used in the literature. Whilst literature usage is not wholly consistent, there is broad consensus on the terms *depleting*, *initial* and *hydrodynamic* microlayer thickness.

Depleting microlayer thickness: The term *depleting* microlayer thickness refers to the instantaneous microlayer profile underneath the bubble. This is the microlayer being depleted by evaporation as the bubble grows, the thickness of which can be measured (e.g. by optical means). In Fig. 2 the *depleting* microlayer is illustrated for one instant in time in the form of a solid line.

Initial microlayer thickness: The term *initial* microlayer thickness is broadly understood as the microlayer thickness when it is first formed at a specific location (Utaka et al., 2014). Qualitatively, this is the thickness of the liquid layer left behind, at point A in Fig. 2, as the steeply sloping ‘forefront’ of the bubble moves radially outwards. It is termed ‘initial’ as evaporation immediately begins to reduce this thickness. Whilst where it starts is inevitably not precisely defined, it is a reasonable and informative measure.

Hydrodynamic microlayer thickness: The terms ‘hydrodynamic’ and ‘isothermal’ have both been used to refer to the microlayer that would form were the bubble to be growing only by vapour evolution from its upper curved surface, and where there was no evaporation from, or thinning of, the microlayer once it had formed (Van Stralen et al., 1975; Jung and Kim, 2018).

2.2. Microlayer experimental observations

By now there are a convincing number of experimental studies that provide sound qualitative, and quantitative evidence regarding microlayers for bubbles under atmospheric steam-water conditions. The experimental difficulties of high temperature and high pressure have caused the majority of single bubble experiments to be limited to atmospheric pressure conditions with a certain range of wall superheats studied. Only one set of measurements (to our knowledge) exists for water at high-pressure. For those the bubble growth rate is seen to be much smaller than at atmospheric pressure, the bubbles tend to remain spherical, and microlayers are not observed (Sakashita, 2011). Some studies with refrigerants have been performed (Schweizer and Stephan, 2009; Stephan et al., 2009) and report a strong evaporation concentrated at the contact line.

The thickness of the microlayer influences the evaporative heat flux that is transported through the bubble base at the wall. However, its high aspect ratio (radial extents of order ~100 times their thickness), the short duration of its existence, its inaccessibility and small size, make measurements of the microlayer very difficult. Consequently, microlayer parameters deduced from experimental observations are generally rather prone to uncertainties.

Some experimental works aim to predict the initial microlayer thickness from the measured temperature variation at the wall surface by calculating the temperature distribution in the solid and the total heat removal (Moore and Mesler, 1961; Hendricks and Sharp, 1964; Yabuki and Nakabeppu, 2014). Other works measure the depleting microlayer thickness directly by using optical meth-

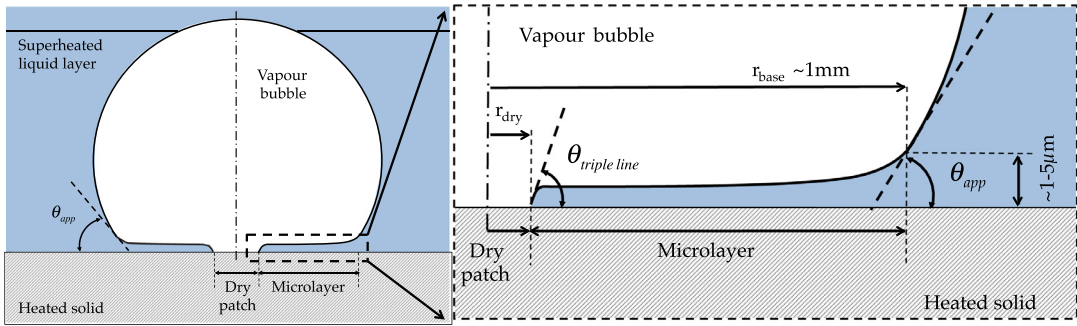


Fig. 1. Microlayer configuration under atmospheric pressure conditions (not to scale).

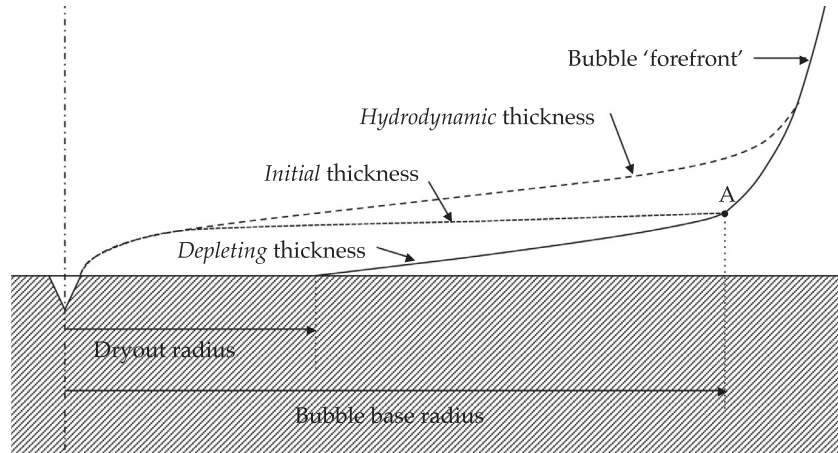


Fig. 2. Schematic of the depleting, initial and hydrodynamic microlayer thickness (not to scale).

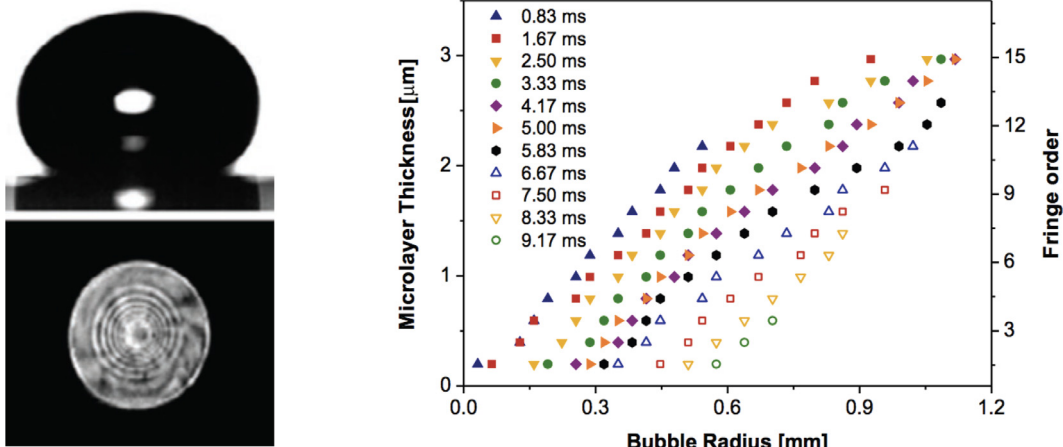


Fig. 3. Left: Typical photo of a steam bubble and measured interference fringe pattern (Jung and Kim, 2014). Right: Derived evolution of depleting microlayer profiles (Jung and Kim, 2014).

ods, such as interferometry (Koffmann, 1980; Koffmann and Plesset, 1983; Kim and Buongiorno, 2011; Jung and Kim, 2014) or the laser extinction method (Utaka et al., 2013), usually combined with high-speed photography. Interferometry methods generate interference fringe patterns, such as the one illustrated in Fig. 3, that are created by the passage of light through the liquid film. From these fringe patterns the thickness and slope of the liquid film can be derived enabling the direct measurement of detailed microlayer profiles and their time history.

Furthermore, more recent progress in synchronized optical and thermal techniques provide even more refined data of microlayers

and the heat transfer processes involved in their evaporation (Jung and Kim, 2014, 2015, 2018).

Various measurements for water at atmospheric pressure at different superheats are listed in Table 1 and illustrated in Fig. 4, and present a reasonably consistent picture of the microlayer configuration.

There are several things to be noted: Only a representative sample of the experimental data is presented here. While, of course, the microlayer changes its radial extent and thickness through time the data given in Table 1 represents just a sample thickness reported in the experiments. Similarly, the wall superheats given in

Table 1

Samples of measured microlayer thicknesses for water at 1 atm.

Experiment	Liquid condition	Wall superheat K	Time ms	Microlayer radius mm	Microlayer thickness μm
Surface temperature methods					
Moore and Mesler (1961)	Saturated	5–16	n/a	0.127	2
Yabuki and Nakabeppe (2014)	Saturated	8	n/a	0.6	3
		15	n/a	0.9	5
Optical methods					
Koffmann and Plesset (1983)	Subcooled	n/a	n/a	0.25	1.85
Kim and Buongiorno (2011)	n/a	n/a	1	1.7	4.8
Utaka et al. (2013)	Saturated	20	n/a	0.39	1.5
Jung and Kim (2014)	Subcooled	22.5	0.83	0.55	2.2
				1.67	0.9
				0.2	3.0
Jung and Kim (2018)	Saturated	9–12	0.4	0.2	1.4
			0.8	0.4	2.3
				0.75	3

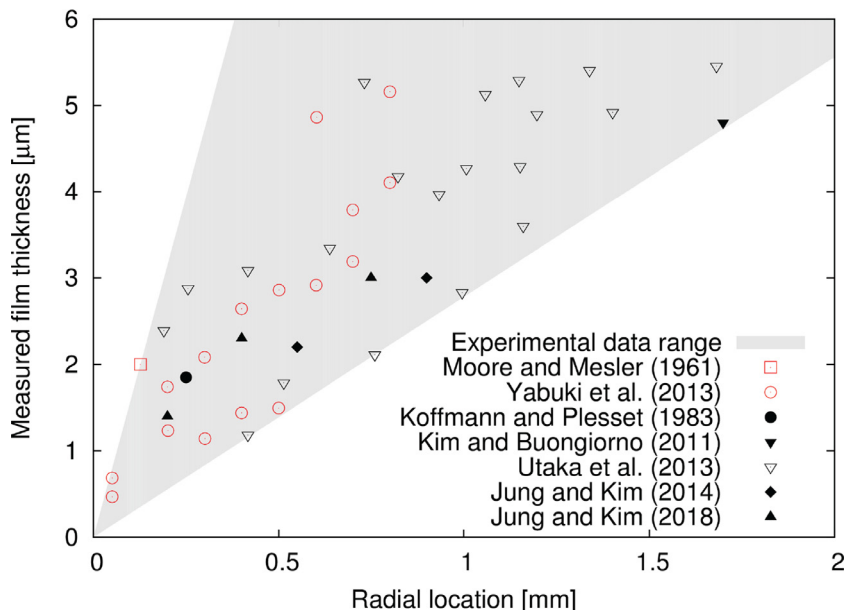


Fig. 4. A representative sample of experimentally-measured microlayer thicknesses for steam-water at atmospheric pressure conditions (red: *initial* thicknesses obtained by surface temperature methods, black: *depleting* thicknesses obtained from optical methods). (For interpretation of the references to colour in this figure legend, the reader is referred to the web version of this article.)

Table 1 are usually just measured in one location at the instant of the bubble's initiation, whereas the wall surface temperature is radially and temporally changing underneath the bubble during its growth.

The contribution of the microlayer to the overall bubble growth is still debated in the literature and indeed its relative importance seems to depend greatly on the particular conditions that obtain. As was mentioned before, microlayers are not observed at all, and their contribution to vapour generation is believed to be minimal under high-pressure conditions (Sakashita, 2011). On the contrary, atmospheric pressure bubbles tend to be much larger by the time they depart, and during their growth do tend to leave microlayers beneath them. The evaporation of these microlayers then plays an important role in the growth and eventual departure of such bubbles (Koffmann and Plesset, 1983; Kim and Buongiorno, 2011; Utaka et al., 2014). It is not clear yet, what is the pressure limit up to which microlayers exist underneath steam bubbles. An understanding of the physical mechanisms that determine microlayer formation is needed. Rather than studying microlayers for one particular condition more can be learned from investigating the microlayer presence and behaviour under a range of conditions (such as a range of pressures and superheats).

Table 2

Microlayer contribution to bubble growth as suggested by experiments with water at atmospheric pressure.

Experiment	Wall superheat K	Microlayer contribution %
Chu et al. (2011)	Not reported	<30
Yabuki and Nakabeppe (2014)	8–15	~50
Utaka et al. (2014)	6–39	15–70
Jung and Kim (2014)	22.5	17

A number of experimental studies have tried to quantify the contribution of microlayer evaporation to the overall bubble growth.

The means by which the fractional contribution of the microlayer was estimated by the individual experimenters varies considerably. The overview given in **Table 2** demonstrates that no consensus has been reached yet. While the work of Utaka et al. (2014) suggests that the wall superheat determines the amount of vapour produced from the microlayer with the contribution increasing with the superheat, Yabuki and Nakabeppe (2014) came to a different conclusion from their data, stating that the microlayer

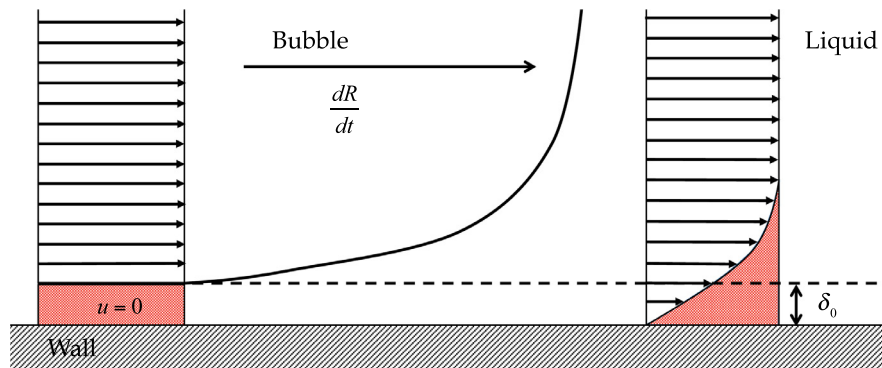


Fig. 5. Schematic of the assumed fluid velocities for the analytical models of microlayer formation (shaded areas have equal sizes).

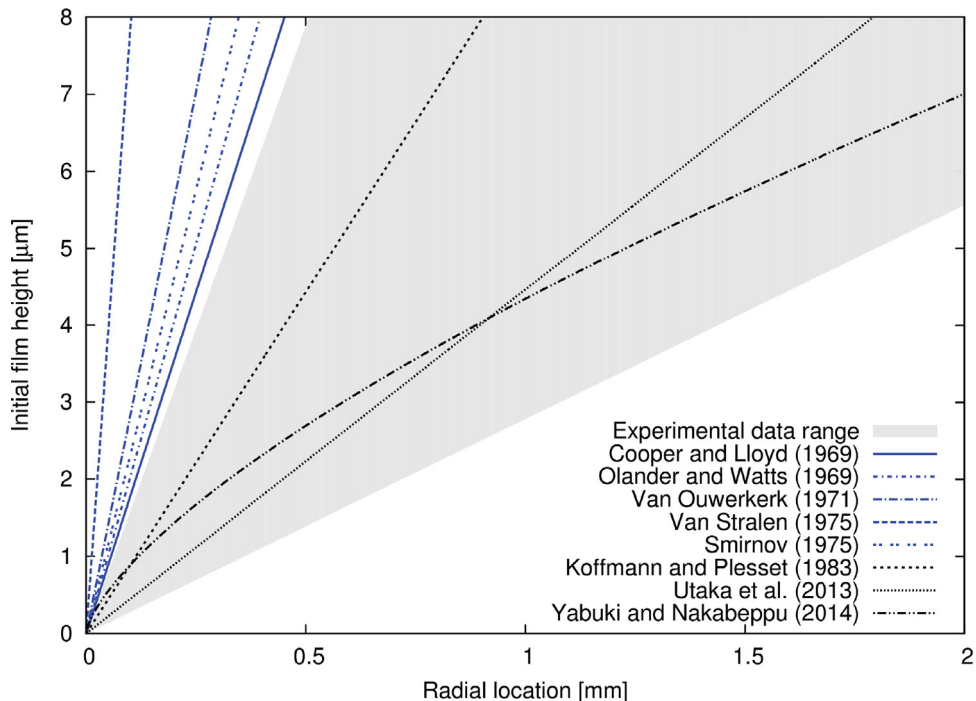


Fig. 6. Comparison of available expressions for the hydrodynamic (blue) and initial (black) microlayer profile for single bubble pool boiling at atmospheric steam-water conditions. The grey area indicates the range of the microlayer thicknesses measured in various experiments, taken from Fig. 4. (For interpretation of the references to colour in this figure legend, the reader is referred to the web version of this article.)

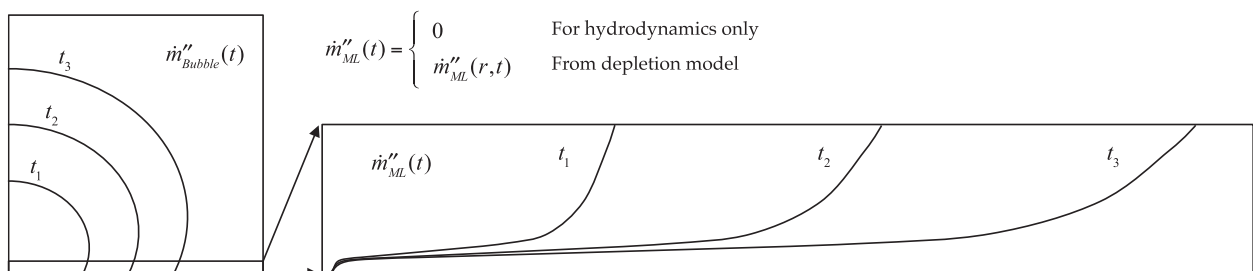


Fig. 7. Schematic of the regions for the evaporation rates for the bubble growth (left) and at the near wall region (inset on the right).

contribution remains constant over the range of wall superheats they investigated.

2.3. Microlayer formation analysis and modelling

There is as yet only a small number of works aiming to add to a better physical understanding of the formation of microlayers

underneath vapour bubbles. The works about microlayer formation generally aim to predict the shape and local thickness of an initial or hydrodynamic film thickness.

2.3.1. 'Physically-based' predictions

Early analytical works (Cooper and Lloyd, 1969; Olander and Watts, 1969; Van Ouwerkerk, 1971; Smirnov, 1975; Van Stralen

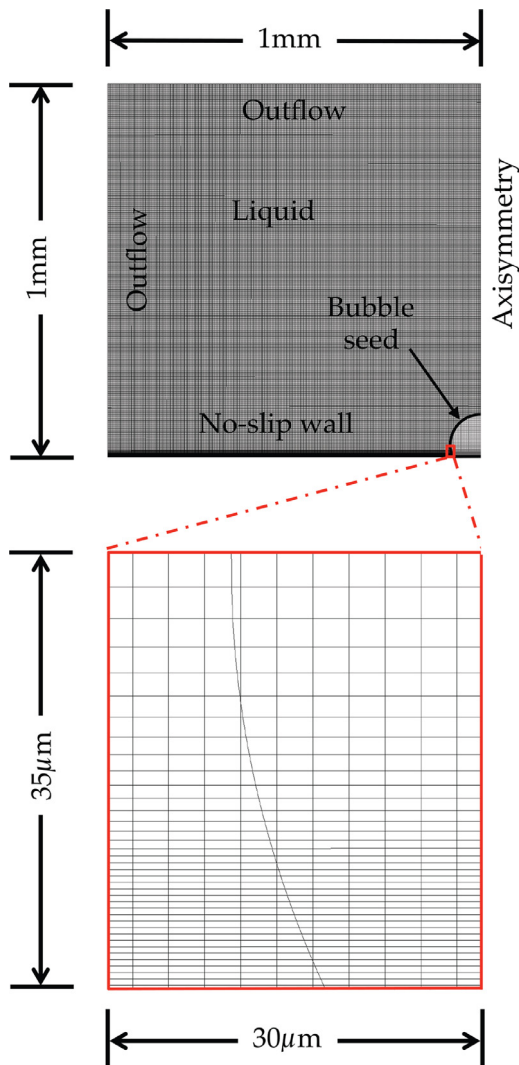


Fig. 8. Top: Computational domain with initial and boundary conditions for the hydrodynamic-only cases. Bottom: Inset of the mesh in the near wall region.

et al., 1975) try to derive an expression for the hydrodynamic microlayer thickness from modelling the flow in the region around the outer edge of the bubble as it expands over the wall. The analyses typically assume a perfect hemispherical shape of the bubble and focus on the pure hydrodynamics of microlayer formation neglecting any depletion by evaporation.

Since the microlayer is very thin compared to the bubble radius, the flow in the microlayer region is considered two-dimensional and lubrication theory applies. Typically, a zero shear condition is applied at the vapour-liquid interface, with a no-slip condition at the wall. In the region in front of the bubble edge a viscous boundary layer has developed at the wall by the expanding bubble pushing the liquid outwards, as illustrated in Fig. 5. Following a hydrodynamic analysis the microlayer thickness is typically found to equal the displacement thickness of the viscous boundary layer.

Since of course the microlayer does not form, and then begin evaporating, as distinct sequential activities, there are some obvious difficulties with this description. The reasonableness of the concept of such hydrodynamic thickness requires that the time to deplete a microlayer be relatively long compared to the time it takes to form it. Given the extremely thin liquid layers observed and the high surface temperatures at the wall, such may well not be the case. In reality a rapid evaporation is likely to start imme-

Table 3
Expressions for the 'hydrodynamic' and 'initial' microlayer thickness.

Analytical expressions (hydrodynamic thickness)	
Olander and Watts (1969)	$\delta_{0,hd} = \frac{\pi}{4\sqrt{3}} \frac{\rho_v h_{fg}}{\rho_l c_{pl} \Delta T} \sqrt{\frac{v_l}{\alpha_l}} r$
Cooper and Lloyd (1969)	$\delta_{0,hd} = 0.8\sqrt{v_l t}$
Van Ouwerkerk (1971)	$\delta_{0,hd} = 1.27\sqrt{v_l t}$
Smirnov (1975)	$\delta_{0,hd} = 1.04\sqrt{v_l t}$
Van Stralen et al. (1975)	$\delta_{0,hd} = 3.632\sqrt{v_l t}$
Empirical expressions (initial thickness)	
Koffmann and Plesset (1983)	$\delta_0 = C\sqrt{v_l t}, \quad C = 0.33 - 0.5$
Utaka et al. (2014)	$\delta_0 = 0.00446r$
Yabuki and Nakabeppe (2014)	$\delta_0 = 0.0005099r^{0.69}$

diate during microlayer formation and while presumably most rapid at the inner, thinner end, will occur over the entire radial extent of the microlayer and influence its formation.

More recently, there have been attempts to model microlayers by means of CFD analyses. Hänsch and Walker (2016) studied the hydrodynamics of microlayer formation using detailed interface-tracking computations. The work of Guion et al. (2018) focused on the hydrodynamic microlayer formation during the very early inertial bubble growth regime. A recent work of Urbano et al. (2018) presents CFD computations of the microlayer formation and evaporation, solving for the temperatures in the fluid region but without incorporating conjugate heat transfer into the solid (Hänsch et al., 2015).

2.3.2. Empirical 'predictive' tools

Most of the recent expressions for the 'initial' microlayer geometry are essentially empirical approaches derived from experimental data of the early bubble growth stage.

Koffmann and Plesset (1983) compared the predictions of the model for the microlayer thickness suggested by Cooper and Lloyd (1969) with their own experimental data for water and ethanol. They suggested a semi-empirical expression for the microlayer thickness. Utaka et al. (2013) performed direct measurements of microlayer profiles for water at atmospheric pressure conditions and derived, by combined analytical modelling and numerical calculations, an expression for the 'initial' microlayer thickness. Using very detailed temperature measurements for isolated bubbles Yabuki and Nakabeppe (2014) derived the spatial distribution of liquid evaporated from the microlayer and arrived at yet another expression for the 'initial' film thickness.

2.4. Comparison of expressions with experimental data

Table 3 lists all the above-mentioned analytical and empirical expressions for the hydrodynamic and initial microlayer thickness suggested in the literature.

Assuming ideal hemispherical bubble growth according to Scriven (1959), and a superheat of 10 K, all the above noted expressions for the microlayer profiles are compared in Fig. 6 for water at atmospheric pressure conditions. Whilst there is not a direct mechanistic correspondence between some measured wall superheat, and a superheat used in a Scriven calculation, the shaded grey region shows observed behaviour over a range of experimental wall superheats from 5 to 22.5 K.

The general observation is that hydrodynamic thickness predictions, derived from pure hydrodynamics, are generally larger than the observed initial thicknesses, derived from actual experimental data. This seems to confirm that evaporation has a marked effect on the microlayer formation process. This is not surprising, as it would be expected that the thinning of the microlayer caused by evaporation would affect its viscous flow behaviour, causing fresh microlayer generated subsequently to be thinner.

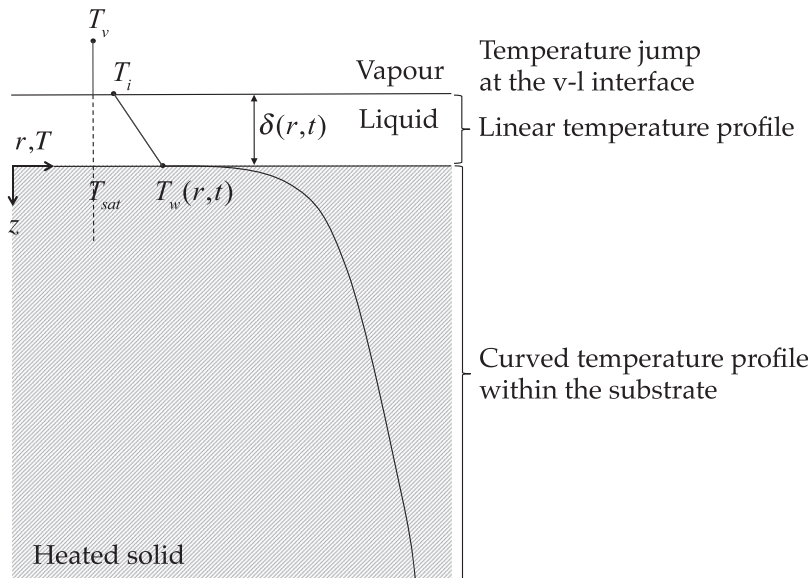


Fig. 9. The form of the temperature distribution in the microlayer and the solid substrate for the adopted microlayer evaporation model (not to scale).

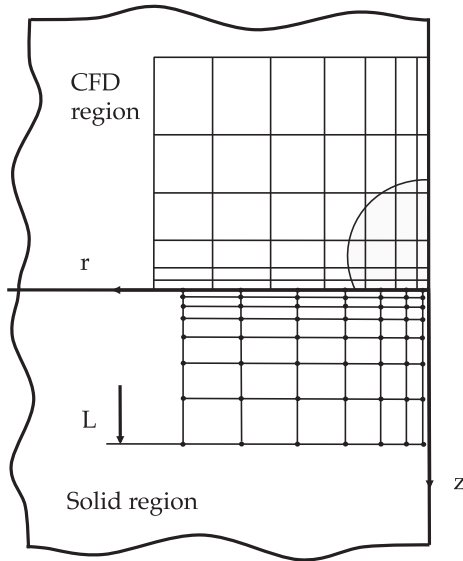


Fig. 10. Relationship between CFD mesh and the 2D axisymmetric heat conduction model solved.

The available models for microlayer formation and evaporation still require proper validation. A problem of all the analytical models for microlayer formation is that they predict a hydrodynamic microlayer thickness that cannot be reproduced in experiments for the simple reason that evaporation cannot be turned off. The empirical models, on the other hand, provide expressions for the initial microlayer thicknesses that are already model-based fits to a particular experiment with a certain set of conditions.

3. The modelling approach

In our analysis a steam bubble is considered to be growing in a stationary pool of liquid. The computational studies are performed using the finite-volume CFD code TransAT (ASCOMP, 2015) operating in an axisymmetric, two-dimensional domain. The two-phase flow formulation in TransAT is based on solving a single set of transport equations for the entire computational domain. The two

phases are treated as a single fluid with variable material properties that change abruptly at the gas-liquid interface. Under the assumption of incompressible, laminar flow the mass and momentum balance is written as:

$$\nabla \cdot \mathbf{u} = \left(\frac{1}{\rho_v} - \frac{1}{\rho_l} \right) \dot{m}'' |\nabla H| \quad (1)$$

$$\rho \frac{\partial \mathbf{u}}{\partial t} + \rho \nabla \cdot \mathbf{u} \mathbf{u} = -\nabla p + \nabla \cdot \mu [\nabla \mathbf{u} + (\nabla \mathbf{u})^T] + \mathbf{f} + \sigma \kappa \mathbf{n} \delta_I \quad (2)$$

To account for the surface tension at the interface, a local term is added to the momentum equation (the last term of Eq. (2)). This surface tension term is computed using the continuous surface force (CSF) model of Brackbill et al. (1992). δ_I denotes a smoothed Dirac delta function centred at the gas-liquid interface.

Note that here we do not solve for the energy balance in the fluid phase. Representation of evaporative mass transfer to model bubble growth and microlayer evaporation will be discussed later.

The different fluids are identified using the level-set method tracking the vapour-liquid interface via a scalar distance function, which is propagated with the fluids:

$$\frac{\partial \phi}{\partial t} + \mathbf{u} \cdot \nabla \phi = -\frac{\rho \dot{m}''}{\rho_v \rho_l} |\nabla \phi| \quad (3)$$

A third-order WENO re-distancing algorithm prevents possible deformations of the level set field due to numerical errors (Sussmann et al., 1994).

3.1. Bubble growth/inflation

We are here primarily concerned with investigating the near wall region, and microlayer formation and evaporation in particular. It is important to ensure that physically realistic bubble growth rates, and in particular physically realistic temporal dependence of these rates, are employed. In order to reproduce such realistic growth rates we prescribe a time-dependent vapour evolution rate to inflate the bubble.

This rate is computed from the classical solution of Scriven (1959). The vapour evolution rate so computed is used to prescribe the time-dependent evolution of vapour from the curved surface of the bubble. This fuels the bubble growth, displacing the vapour-liquid interface near the wall at realistic rates.

Table 4

The physical properties used for the fluid and solid region.

Physical property	Unit	Material		
		Water at 1 bar		Solid
		Liquid	Vapour	CaF ₂
σ	N/m	0.0589		
h_{fg}	kJ/kg	2257		
T_{sat}	K	373.15		
μ	μPas	277	12.55	
ρ	kg/m ³	958	0.579	3180
c_p	J/kgK	4220	2030	854
λ	W/mK	0.679	0.025	9.71

Table 5

Mesh characteristics for the grid convergence study.

Grid	Cell number	Δx_{min}
Coarse	100 × 100	4 μm
Mid	200 × 200	2 μm
Fine	350 × 350	1 μm

Table 6

Parameters for the grid convergence study of the depleting film case.

Grid	Near-wall Δx [μm]	Cells in initial liquid film
60	1.6	4
120	0.8	8
240	0.4	16
480	0.2	32

There is no direct and mechanistic connection between the superheat applied in the Scriven model and the superheat of the heating surface in the experiment, although the values are not dissimilar. Rather, a value was selected for the Scriven calculation that caused overall bubble volume versus time to match that observed experimentally, thus providing a representative context in which to perform the focussed study of microlayer behaviour.

In our computations the Scriven-derived evaporation rate is applied to the curved surface of the bubble but not to the microlayer. The vapour generation from the microlayer is computed mechanistically via the microlayer depletion model that will be described fully below. This is illustrated schematically in Fig. 7.

3.2. Hydrodynamic formation of a microlayer

For the CFD calculations of the pure hydrodynamic formation of microlayers the evaporation rate applied to the curved surface is set to zero in the near wall region ten microns above the wall, allowing the unaffected formation of the microlayer based on the Navier-Stokes equations.

The actual nucleation process is not modelled, but is imposed via the initial specification of a small vapour seed in the centre of the domain. Typically the seed is taken to be a few cells in size, but predictions are not sensitive to this choice. As this bubble seed grows radially outwards, liquid is displaced, with a no-slip boundary condition at the wall.

The computational domain with initial and boundary conditions is illustrated in Fig. 8. The mesh was greatly refined in the near wall region to allow for the resolution of the microlayer potentially forming underneath the bubble.

An initial report of modelling the hydrodynamics of the microlayer formation has been presented earlier (Hänsch and Walker, 2016). Validation of these initial results will be given in 4.1, and an extension of these results to model up to the point of bubble departure, will be presented in Section 5.1.

3.3. Specification of a contact angle

In the computations presented here there is no imposition of an ‘apparent’ contact angle (recall the various contact angles illustrated in Fig. 1). This contact angle is automatically computed, as the shape of the interface throughout the bubble base region is part of the CFD solution. The only place where there is even any opportunity to impose some model of the interaction between the vapour, liquid and solid is at the inboard end of the microlayer, at the triple line.

It is not practicable to measure the contact angle at the radially-inboard end of the microlayer, so this can provide no real guidance to modelling.

Understanding of the physics of the wetting/drying process during nucleate boiling is still limited (DasGupta et al., 1993, DasGupta et al., 1994, Mitrovic, 1997, Phan et al., 2009), and on the length scale of the detailed study here real surfaces will not be at all flat anyway, adding further difficulties to the specification of a ‘contact angle’.

The important issue here is what representation to include in the code to reflect best the behaviour on the length scale being modelled. Specification of an equilibrium contact angle is required by the CSF model in order to calculate the interface normal vector to the wall. Lacking justification for anything different, the condition chosen was neutral, neither hydrophilic nor hydrophobic; that is such as to present no resistance or encouragement to the motion of the contact line, and not influencing the force balance applied in the CFD solution.

However, given the aspect ratio of the microlayer, which is possibly hundred times greater in radial extent than thickness, the details of this treatment anyway were found to have little practical effect (an observation also of Guion, 2017), although it is an area that it would be interesting to study further.

3.4. The microlayer evaporation model

The boundary conditions adopted are saturation temperature inside the bubble, and an adiabatic boundary deep in the substrate. Initial conditions take all the substrate to be at a uniform temperature.

The thermal capacity of the substrate is important, and the evolving temperature within the substrate is found by solving the transient heat conduction equation. The two-dimensional axisymmetric heat conduction within the solid is solved using cylindrical coordinates via the finite-difference method, allowing unequal discretization in the radial and axial direction.

Whilst the radial flow of liquid in the microlayer is computed mechanistically, via solution as normal of the highly resolved Navier Stokes equations, the radial flow is neglected in the computation of the depletion of the microlayer. The thermal capacity of the liquid layer is negligible (or equivalently, the thermal penetration depth into the substrate is many times the microlayer thickness for the relevant temporal rates of change), and the temperature profile within the microlayer is thus taken to be linear.

The resistance to the flow of heat presented by the very thin microlayer is very small, to the extent that the thermal resistance offered by the evaporative process itself can become comparable. This effect was brought to light by anomalous results that were observed experimentally (Jung and Kim, 2015), and that were explained by an analysis that incorporated this evaporative thermal resistance (Giustini et al., 2016). Accordingly, we incorporate in our microlayer depletion model the same representation of thermal resistance as was demonstrated to resolve this issue. Based on the work of Schrage (1953) we incorporate an evaporative heat trans-

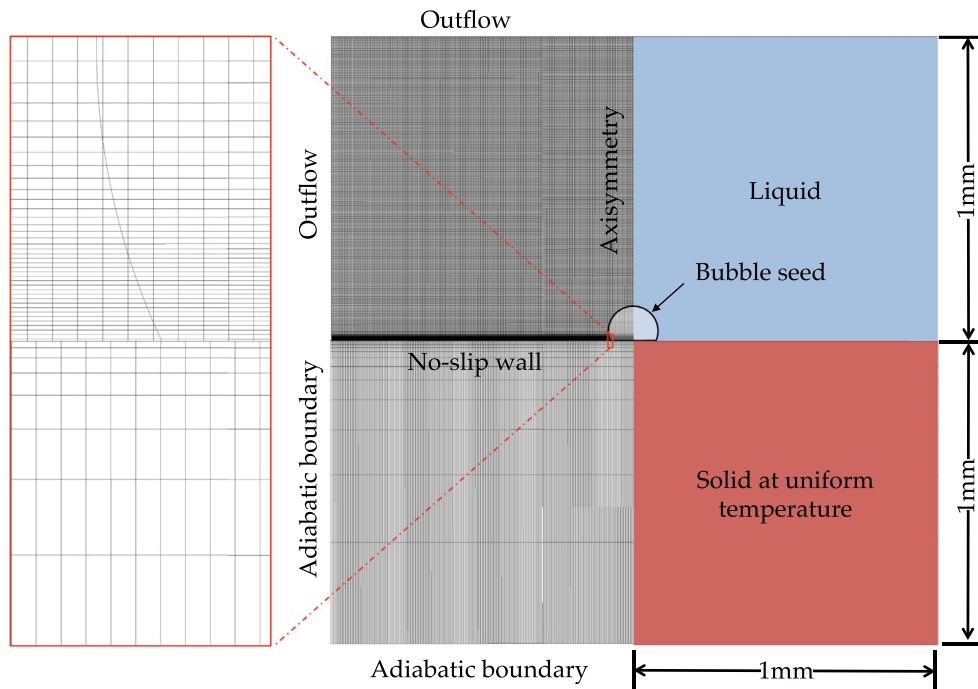


Fig. 11. Left: Computational domain for the CFD region and the modelled solid region (zoomed-in inset for a radial extent of $30\text{ }\mu\text{m}$ reaching $35\text{ }\mu\text{m}$ into each the fluid and the solid region). Right: Initial conditions.

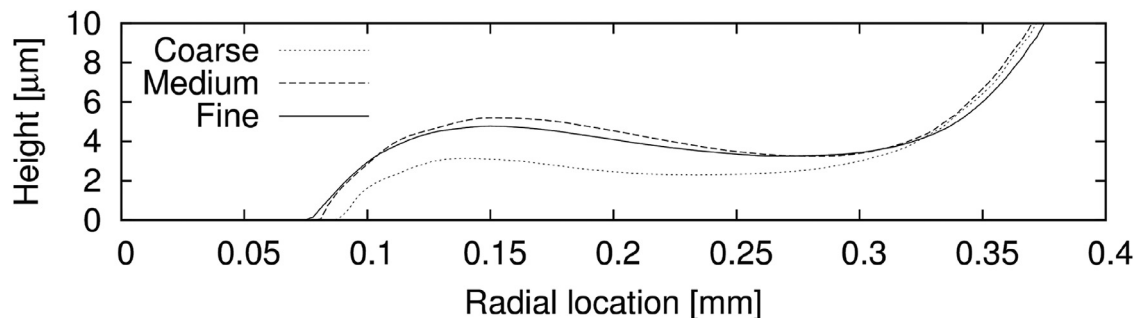


Fig. 12. Grid convergence study for Rate 2 showing the predicted microlayer profiles after 0.5 ms ([Hänsch and Walker, 2016](#)).

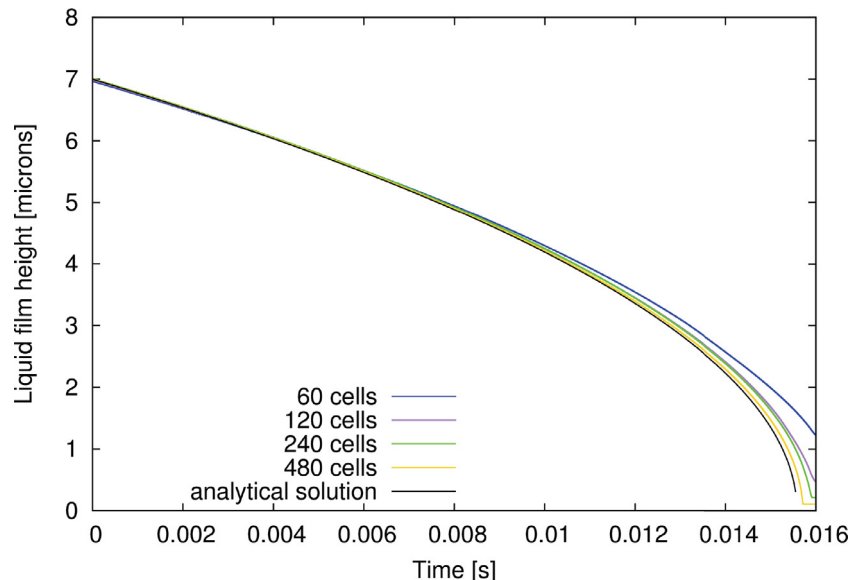


Fig. 13. Evolution of the liquid film height for different grids compared to the analytical solution.

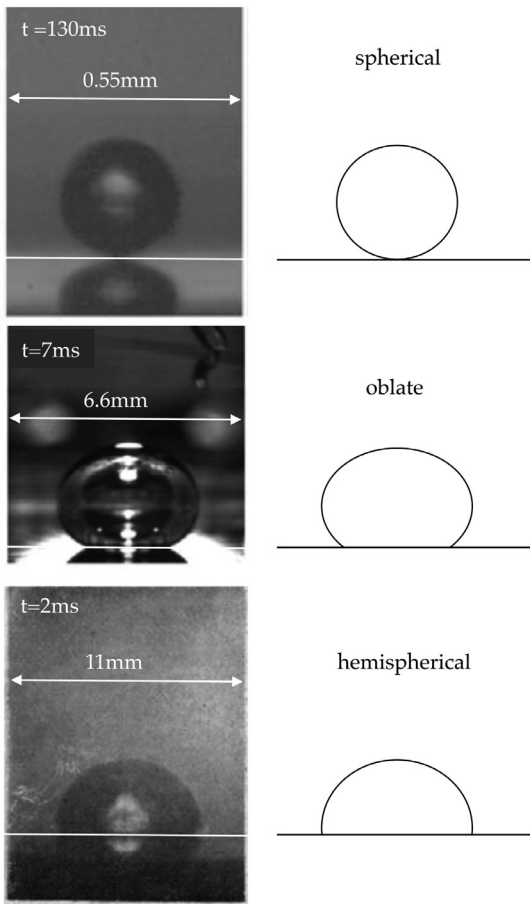


Fig. 14. Typical experimental images of bubble shapes at different growth rates. Top: high-pressure bubble (at 2.70 MPa) with ‘slow’ growth rate (Sakashita, 2011). Mid: atmospheric-pressure bubble with ‘medium’ growth rate (Yabuki et al., 2013). Bottom: low-pressure bubble (at 0.03 MPa) with a ‘fast’ growth rate (Johnson et al., 1966).

Table 7
Parameters for the three bubble growth rates considered.

Parameters	Unit	Rate 1	Rate 2	Rate 3
Sciven ΔT	K	5	10	15
Growth constant β		15.0	29.6	44.3
Ja number		15.4	30.9	46.4
Simulation specifications				
Seed radius	μm	30	80	140
Initial time	μs	5.9	10.8	14.9
Initial $\dot{m}_{\text{Bubble}}''$	kg/m ² s	1.46	2.14	2.73

fer coefficient at the vapour-liquid interface:

$$h_{lv} = \frac{2a}{2-a} \frac{h_{fg}^2 \rho_v}{\sqrt{2\pi R_{\text{gas}} T_{\text{sat}}^{\frac{3}{2}}}} \quad (4)$$

This involves an ‘accommodation coefficient’ a , which is a measure of the fraction of the evaporating liquid molecules that remain within the vapour phase having once escaped from the liquid. Its value was inferred (Giustini et al., 2016) from the experiments noted (Jung and Kim, 2015) to be ~ 0.02 , a value itself broadly consistent with literature values between 0.1 and 0.01 of this rather elusive quantity.

The net result is a transient temperature distribution of the form shown in Fig. 9, with a sharp jump at the vapour-liquid interface, a linear variation of temperature through the microlayer, and an error function-like variation down into the substrate.

The evaporative heat flux from the microlayer, incorporating the evaporative resistance, is given by:

$$\dot{q}_{ML}'' = \frac{T_w(r, t) - T_{\text{sat}}}{\frac{\delta(r,t)}{\lambda_i} + \frac{1}{h_{lv}}} \quad (5)$$

The rate of heat transfer to the vapour-liquid interface determines the vapour production rate there, via:

$$\dot{m}_{ML}'' = \frac{\dot{q}_{ML}''}{h_{fg}} \quad (6)$$

This vapour is then added to the computational cells lying along the vapour-liquid interface.

3.5. Coupling of the evaporation model with the CFD analysis

The above microlayer evaporation model has been coupled to the interface-tracking code TransAT, via additional coding. Fig. 10 demonstrates the relationship between the CFD mesh and the modelling applied to the substrate, as described above.

The CFD cell at each radial location is associated with a node in the unsteady heat conduction model for the substrate. This heat conduction model in the solid propagates up to a specified length L , with a suitably graded mesh, to capture the thermal disturbance of the substrate.

The computational process is as follows:

During the initialisation stage the number and location of the radial grid points is detected from the CFD mesh and a corresponding solid grid is established. During the CFD simulation for each time step the current time, time step size and level set field are read from the CFD analysis, and are taken into the microlayer model, in which the following steps are performed:

1. At each radial location the current microlayer height is calculated from the level set data of the CFD solution.
2. The evaporative mass transfer rate is calculated according to Eq. (6) for each radial location. For this computation the wall surface temperature calculated by the heat conduction part of the code at the previous time step is used.
3. The gas-liquid interfacial area is computed for each radial location.
4. A wall heat flux is calculated based on the wall face area and the interfacial area at each radial location.
5. The (radially-varying) wall heat flux then serves as an upper boundary condition for the solid heat conduction domain in order to solve for the solid temperatures at the next time step, via implicit time-stepping.

The computed mass transfer rates for all microlayer cells are given back as output values to the CFD code. It is then converted into a volumetric vapour source, which is applied to the near-wall cells.

3.6. Computational domain

The domain used for the computational studies, including the microlayer evaporation discussed above, is illustrated in Fig. 11.

An adiabatic underside to the substrate was imposed, but with the substrate thickness taken as several times the thermal penetration depth the boundary condition adopted makes no material difference.

The mesh of the CFD region was greatly refined close to the wall, where the focus of our computational studies lies. Similarly the grid of the solid domain was refined towards the liquid-solid surface. The grid convergence study will follow in Section 3.7.

Adaptive time-stepping was employed, to stay within bounds for the CFL number, and diffusion and surface tension criteria

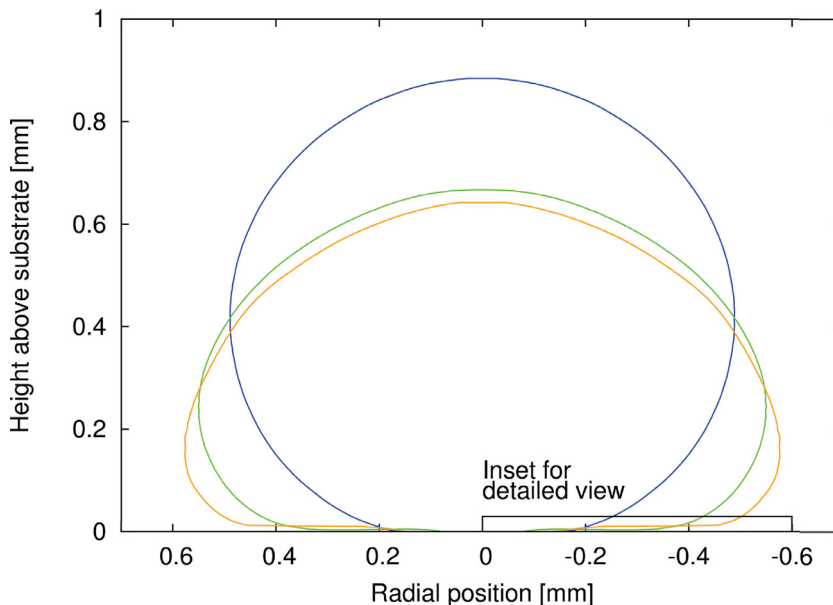


Fig. 15. Comparison of bubble shapes for three growth rates, at the same bubble equivalent radius of 0.6 mm, after 1.84 ms for Rate 1 (blue), 0.5 ms for Rate 2 (green) and 0.21 ms for Rate 3 (yellow) (re-drawn from Hänsch and Walker, 2016). (For interpretation of the references to colour in this figure legend, the reader is referred to the web version of this article.)

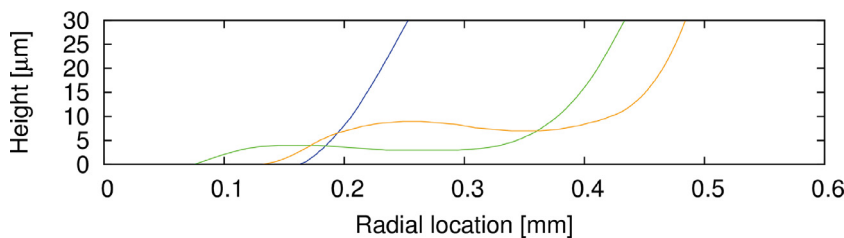


Fig. 16. Detailed view showing the interface outlines for Rates 1, 2 and 3 at the same bubble equivalent spherical diameter. Blue: Rate 1 at 1.84 ms, Green: Rate 2 at 0.5 ms, Yellow: Rate 3 at 0.23 ms (re-drawn from Hänsch and Walker, 2016). (For interpretation of the references to colour in this figure legend, the reader is referred to the web version of this article.)

Table 8

Parameters used for the simulation of the experimental case 1 (Rate 4).

Parameters	Rate 4
Growth constant β	54.6
Ja number	57.2
Simulation specifications	
Seed radius [μm]	185
Initial time [μs]	17.08
Initial vapour evolution rate [$\text{kg}/\text{m}^2\text{s}$]	3.13

(ASCOMP, 2015). Typically, time steps of $\sim 2\text{ ns}$ were required to converge the solution. This very small time step was a major contributor to the computational difficulties; whilst a large cluster was used, the benefits of multiple processors are small when high computational demands stem from large numbers of time steps.

The fluid and solid properties applied for the following computational studies are listed in Table 4.

3.7. Verification

For a first grid convergence study the hydrodynamic microlayer formation for the vapour generation with Rate 2 was simulated. Three different grids, listed in Table 5, were employed. While the evolution of the overall bubble shape for the three different mesh sizes is essentially identical, the main effect of refining the mesh

becomes visible near the wall. Fig. 12 plots the microlayer profiles for each grid size after 0.5 ms. Note that due to the slender aspect ratio of the microlayer its graphical representation needs to use very different radial and axial scales, or nothing of interest would be visible. The comparison shows that the microlayer shape and thickness is reasonably grid-convergent for the two finer meshes employed.

Various test cases were studied for the combined formation-depletion model, of which a verification test case for the correct depletion of the vapour-liquid interface will be presented here.

A test case was set up in order to investigate the depletion of a $7\ \mu\text{m}$ -thick liquid film close to the wall when coupled to the microlayer evaporation model.

At the wall a pseudo-Dirichlet boundary condition was applied by increasing greatly the solid thermal conductivity, so the wall surface temperature was maintained at a constant value of 5 K. Assuming perfect evaporation (a point to which we will return) an analytical solution exists for the temporal variation of the liquid film thickness.

A grid convergence study was performed with the four different grids listed in Table 6.

Good convergence to the analytical solution with the different grids is demonstrated in Fig. 13.

Following these grid convergence studies for both the formation and depletion of a microlayer, a CFD grid of 350×350 cells and a solid grid of 350×16 cells were adopted, with mesh sizes of $\sim 0.5\ \mu\text{m}$ at the liquid-solid surface.

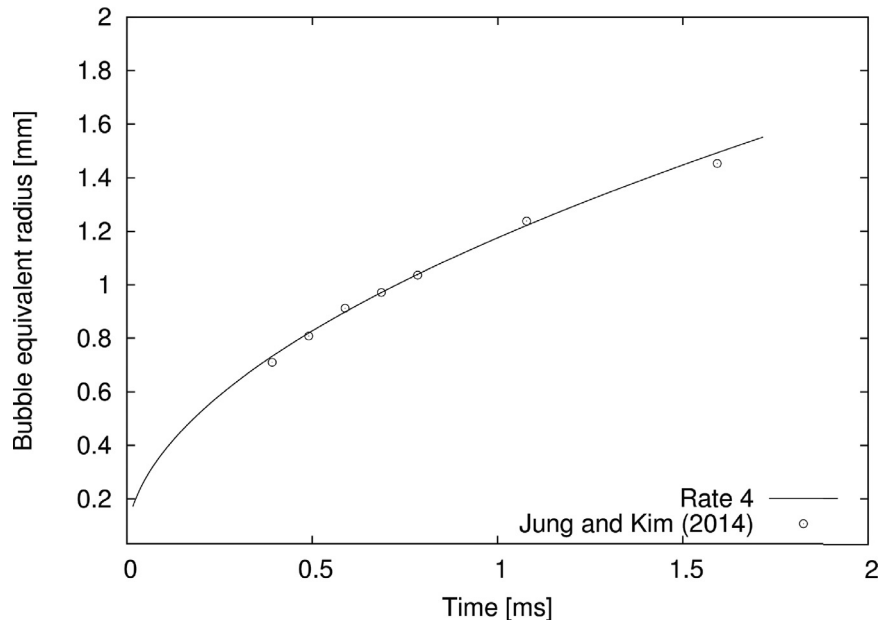


Fig. 17. Bubble growth rate used in the computations, selected to reproduce the bubble growth rate observed in the measurements of Jung and Kim (2014).

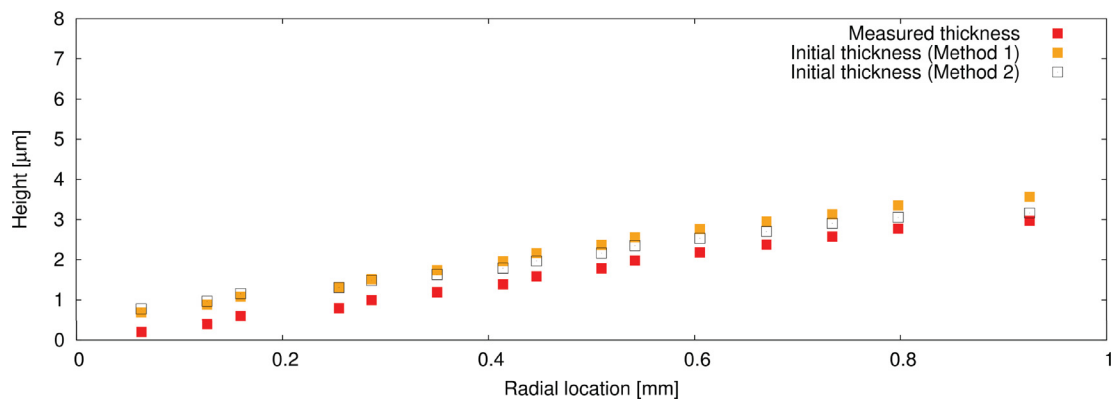


Fig. 18. Measured depleting and inferred initial microlayer thickness after 1.67 ms.

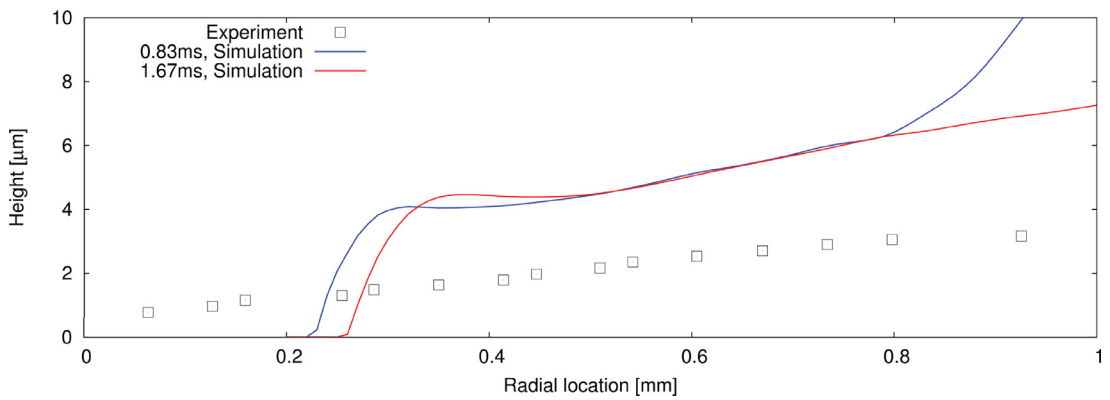


Fig. 19. Comparison of the inferred initial microlayer thickness to the computational results after 0.83 ms and 1.67 ms.

4. Validation

Modelling of a properly posed microlayer generation and depletion problem requires specification of:

- The physical properties of the substrate and the fluid at the operating conditions.

- The initial temperature distributions within both the solid and the liquid surrounding the bubble.
- The temperature (or heat flux) boundary conditions throughout the time of interest.
- The initial velocity and pressure field within the liquid surrounding the bubble.

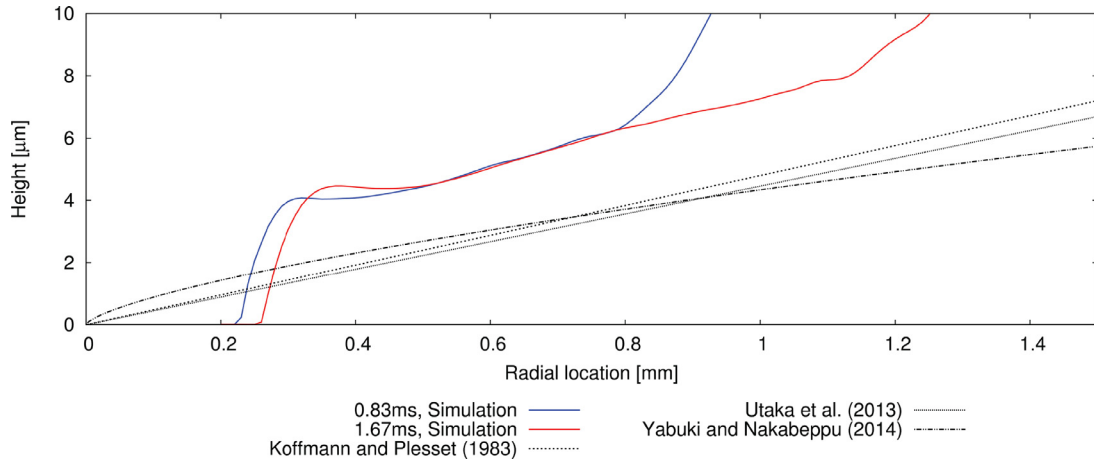


Fig. 20. Comparison of the results with empirical expressions for the initial microlayer thickness.

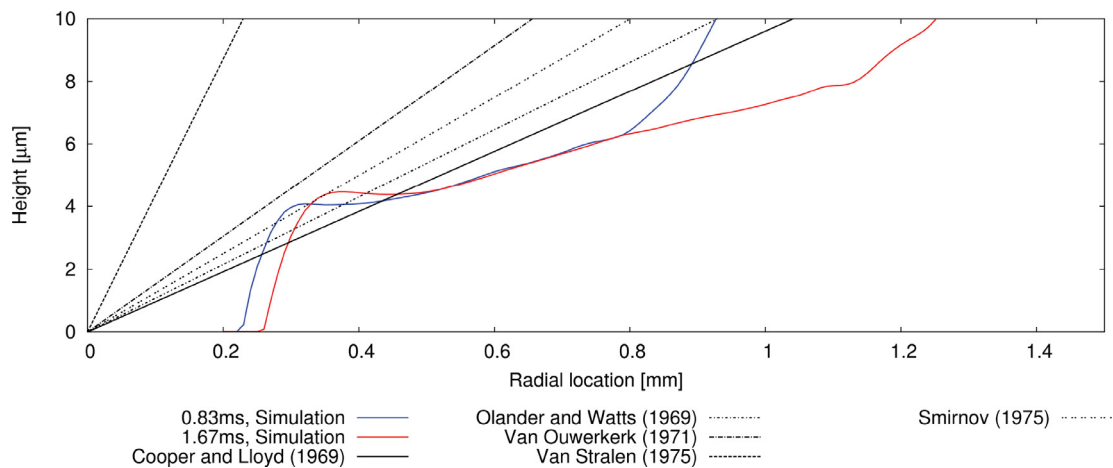


Fig. 21. Comparison of the results with analytical expressions for the hydrodynamic microlayer.

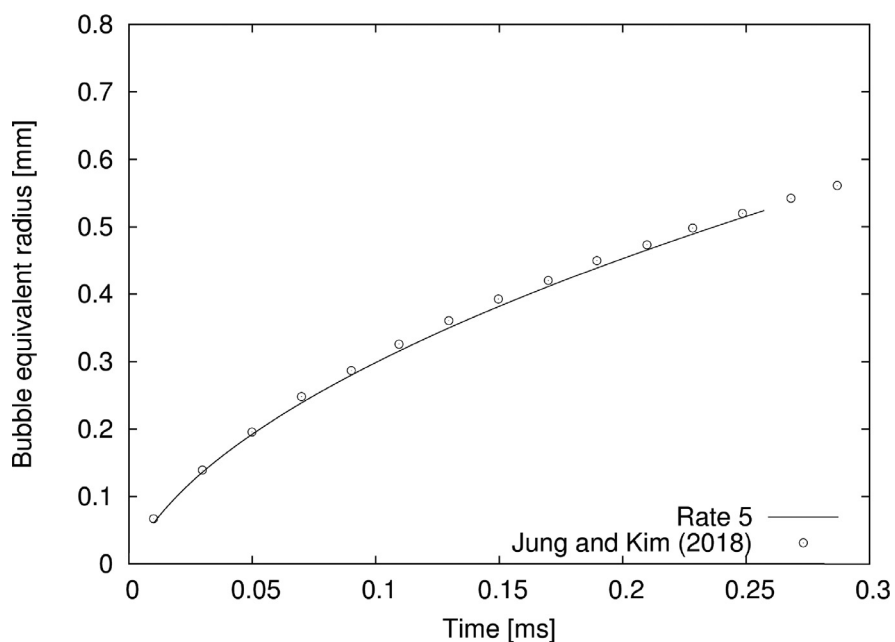


Fig. 22. Computed bubble growth rate with Rate 5 compared to the measurements of Jung and Kim (2018).

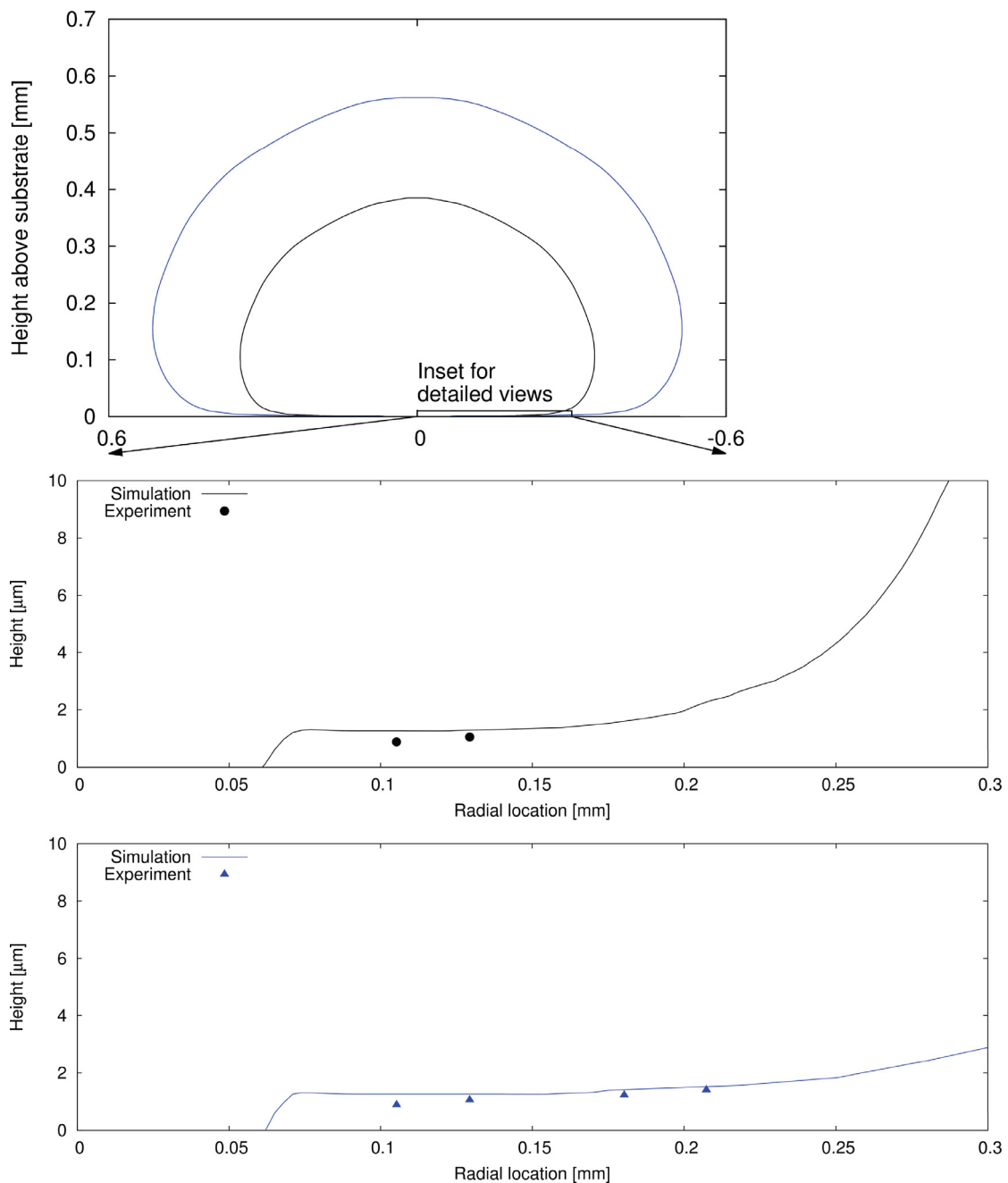


Fig. 23. Top: Predicted bubble shapes after 0.1 ms and 0.2 ms. Below: Comparison between measured and predicted microlayer profiles when including microlayer evaporation after 0.1 ms (middle) and 0.2 ms (bottom).

- The velocity and pressure boundary conditions throughout the time of interest.
- For the validation of the CFD predictions it is then desirable to know ‘consequent’ quantities such as:
- The transient temperature distribution over the liquid-solid interface.
- The transient temperature distribution within the surrounding liquid.
- The bubble growth rate and the velocity field in general.
- The transient bubble shapes.
- The microlayer radial and temporal thickness variation.

The above-listed data that need to be measured, both to define a properly posed problem and to allow evaluation of the quality of

predictions, are extremely challenging to obtain. There is no measurement of which we are aware that allows such a properly posed problem to be identified. That comment is, we hope obviously, not meant in the slightest as a criticism of the experiments. Recall, these experiments are taking place in regions of order 1 mm in size, observing events that take place over periods of order a few milliseconds, and furthermore, within this, our prime interest here is in microlayers that have thicknesses between zero and 5 μm . It does, though, mean that validation of predictive models is necessarily constrained.

In what is probably the most comprehensive set of measurements [Jung and Kim \(2014\)](#), and more recently [Jung and Kim \(2018\)](#), have investigated microlayers in water at atmospheric

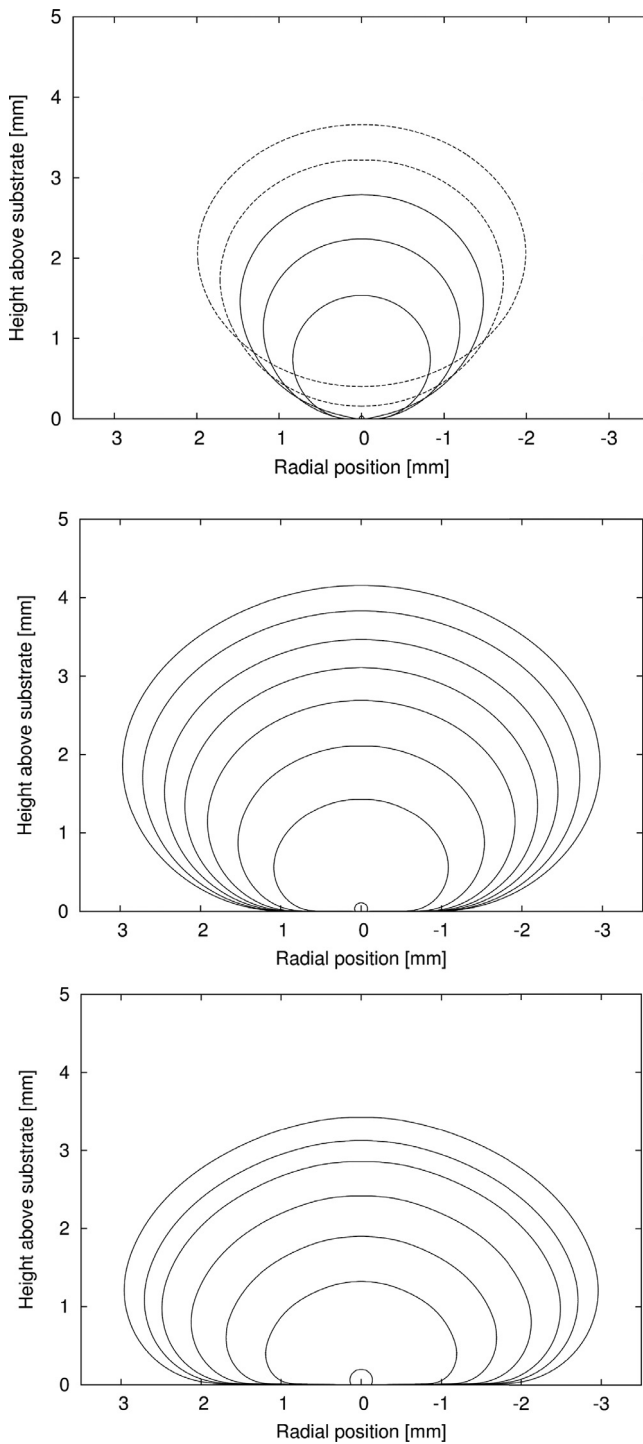


Fig. 24. Evolution of bubble shapes for a typical ebullition cycle. Top: Rate 1 after 0 ms, 5 ms, 10 ms, 15 ms, 20 ms and 25 ms. Middle: Rate 2 after 0 ms, 2 ms, 4 ms, 6 ms, 8 ms, 10 ms, 12 ms and 14 ms. Bottom: Rate 3 after 0 ms, 1 ms, 2 ms, 3 ms, 4 ms, 5 ms and 6 ms.

pressure. They used interferometry to obtain the time histories of microlayer profiles, infrared measurements of the wall surface temperature, and high-speed photography to determine the bubble shapes and growth rates. As this is the most complete experimental data to date we will try to validate our CFD predictions with it to the degree possible.

We will try to validate both the hydrodynamic-only computations, and the results including the evaporation from and corresponding depletion of the microlayer, in the next two sections.

4.1. Hydrodynamic-only

We validate our hydrodynamic-only predictions in two steps. First, we make largely qualitative comparisons of the predicted bubble shapes and the prediction or not of the formation of microlayers at the bubble base with general observations made in experiments. Second, an experimental case is reproduced and the predicted hydrodynamic microlayer profiles are compared to the measured data, albeit this measured data, for conditions where evaporation is depleting the microlayer, will need considerable modification. We will also make comparison with analytical models that have been suggested in the literature.

4.1.1. Qualitative

In experimental studies of bubble growth it is generally observed that at high pressure, or low bubble growth rates (low superheat), bubbles remain essentially spherical. These spherical bubbles seem barely to touch the wall and microlayers have not been reported (Sakashita, 2011). At lower pressures, or higher growth rates, the observed bubble shapes become more oblate (Yabuki et al., 2013), and even tend toward a hemispherical shape at the highest growth rates (Johnson et al., 1966). Such oblate and hemispherical bubbles do tend to leave microlayers beneath them (Jung and Kim, 2014, 2018).

The observed bubble shapes at these different growth rates are illustrated in Fig. 14. Note the large range in parameters. The photographs below range in time from 2 ms to 130 ms after nucleation, and the volume ratio of the bubbles depicted is approaching 10,000.

These qualitative observations are reproduced by hydrodynamic-only calculations (Hänsch and Walker, 2016).

Three growth rates were employed, achieved by the use of three superheat levels incorporated into the Scriven vapour generation model. These are identified in Table 7.

Fig. 15 re-drawn from Hänsch and Walker (2016), illustrates the bubble shapes predicted by the different bubble growth rates in those computations, here drawn at the same bubble equivalent diameter. The slow growth rate is seen to produce a generally spherical bubble, whereas at the medium rate the bubble assumes an oblate shape. The fastest growth rate produces a bubble shape that tends towards a hemisphere. The near-wall region is illustrated in more detail in Fig. 16. It is seen that essentially no microlayer is predicted underneath the bubble at a slow growth rate. A microlayer is formed for the other two cases, with an increase in both radial extent and thickness of the microlayer with increasing bubble growth rate. This is all consistent with the general trend of bubble growth rate and shape observations made in the above-mentioned experiments.

4.1.2. Quantitative comparison of microlayer profiles

For a validation case we adopt the conditions in the experiment of Jung and Kim (2014) and compare our predictions to these measurements. A bubble growth rate was selected to give a temporal dependence of the bubble volume (or equivalent radius) close to that measured in the experiment. This is shown in Table 8 and Fig. 17.

We cannot, of course, compare the observed microlayer profiles of Jung and Kim (2014) with those predicted from the hydrodynamic-only model; the microlayers are observed as they are simultaneously being depleted by evaporation.

To make a comparison possible we will attempt to “replenish” the experimentally-observed microlayers by computing the deple-

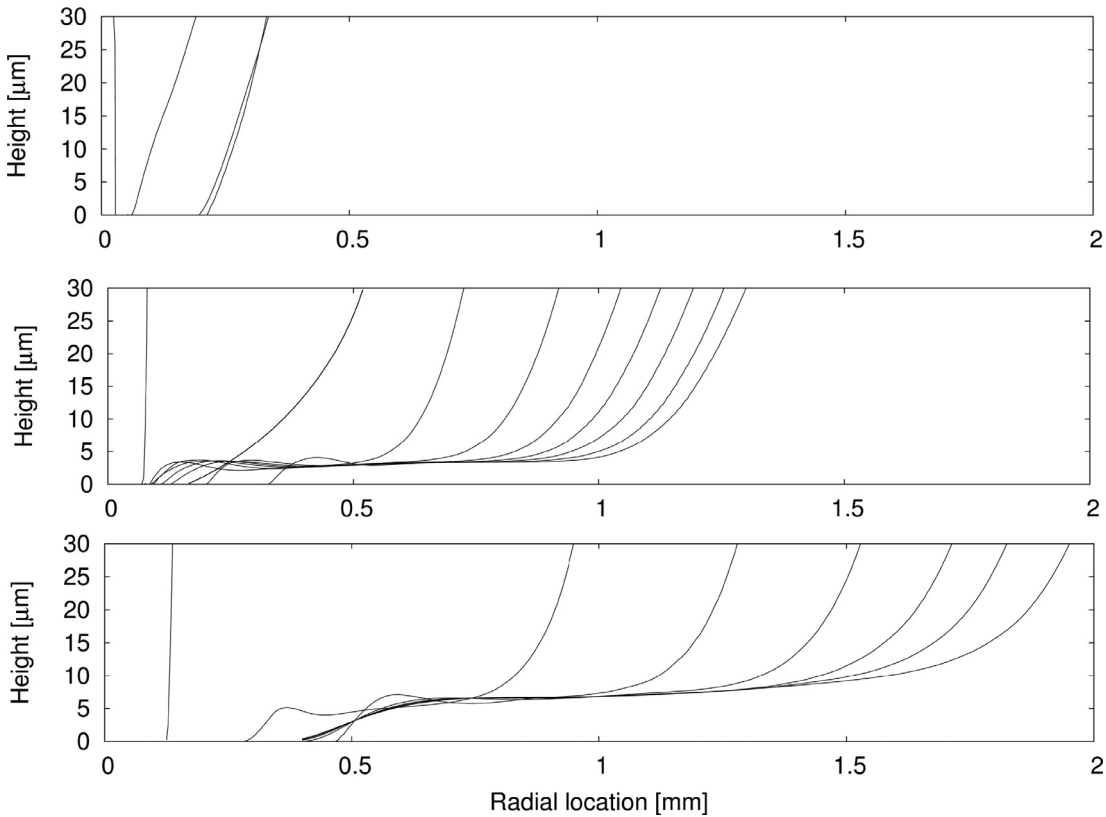


Fig. 25. Evolution of microlayer profiles for a typical ebullition cycle. Top: Rate 1 after 0 ms, 5 ms, 10 ms and 15 ms. Middle: Rate 2 after 0 ms, 2 ms, 4 ms, 6 ms, 8 ms, 10 ms, 12 ms and 14 ms. Bottom: Rate 3 after 0 ms, 1 ms, 2 ms, 3 ms, 4 ms, 5 ms and 6 ms.

tion to which they have been subject. Such an approach has a long history in the literature, notably having been employed by Moore and Mesler (1961), Utaka et al. (2014) and Yabuki and Nakabeppe (2014).

From the experimental data we try to infer an *initial* microlayer thickness. Two different approaches can be used, which will be described here briefly.

Method 1

An initial microlayer thickness can be inferred from the (time and position dependent) measured thickness and the measured liquid-solid interface temperature.

At any instant we have that the rate of reduction of microlayer thickness is given by:

$$\rho_l h_{fg} \frac{d\delta}{dt} = - \frac{T_w(t) - T_{sat}}{\frac{\delta(t)}{\lambda_l} + \frac{1}{h_{lv}}} \quad (7)$$

where the second term in the denominator incorporates the imperfect evaporation discussed above. It is calculated by Eq. (4) with the accommodation coefficient $a=0.02$ as suggested by Giustini et al. (2016).

Integration then gives the change in thickness from the initial thickness to the observed value:

$$\int_{\delta_0}^{\delta(\tau)} \left(\frac{\delta(t)}{\lambda_l} + \frac{1}{h_{lv}} \right) d\delta = - \int_0^\tau \frac{(T_w(t) - T_{sat})}{\rho_l h_{fg}} dt \quad (8)$$

Evaluation of this allows the initial microlayer thickness to be evaluated from the observed, depleted thickness.

Method 2

A second method of inferring the degree of depletion from the initial microlayer thickness to the observed thickness is based on only the measured radially and temporally varying surface tem-

perature data. A heat conduction analysis in the substrate is performed, applying the measured wall temperature as a transient boundary condition.

This allows the spatially and temporally varying total heat removal from the solid to be computed, via

$$\delta_0 - \delta(\tau) = \frac{\rho_s c p_s}{\rho_l h_{fg}} \int_0^L (T_s(t=0, z) - T_s(t=\tau, z)) dz \quad (9)$$

and from this the degree of depletion is able to be determined at each radial location.

Application of these two methods, using observations at 1.67 ms, is shown in Fig. 18. Subject to experimental uncertainties, the initial microlayer profiles inferred by the two approaches should be the same, and indeed good agreement is apparent.

Note that this evaluation has included representation of evaporative resistance. This is a point we will return to in Section 5.2.2.

4.1.3. Comparison of the hydrodynamic-only prediction with the ‘replenished observation’ of initial thickness

Using the inferred values from the previous section, we show in Fig. 19 the computed hydrodynamic microlayer profiles, and the initial thickness profile. Note the very different horizontal and vertical scales in those graphs.

Both the experiment and our calculations predict microlayer profiles with a slope of ~ 0.004 – 0.005 . As expected the hydrodynamic microlayer profiles predicted by our CFD calculations exceed the initial microlayer thicknesses inferred from the measurements. Just as was the case for the analytical models shown in Fig. 6, it is seen that pure hydrodynamics predict microlayers that are generally thicker than initial microlayers inferred from experimental data under evaporating conditions.

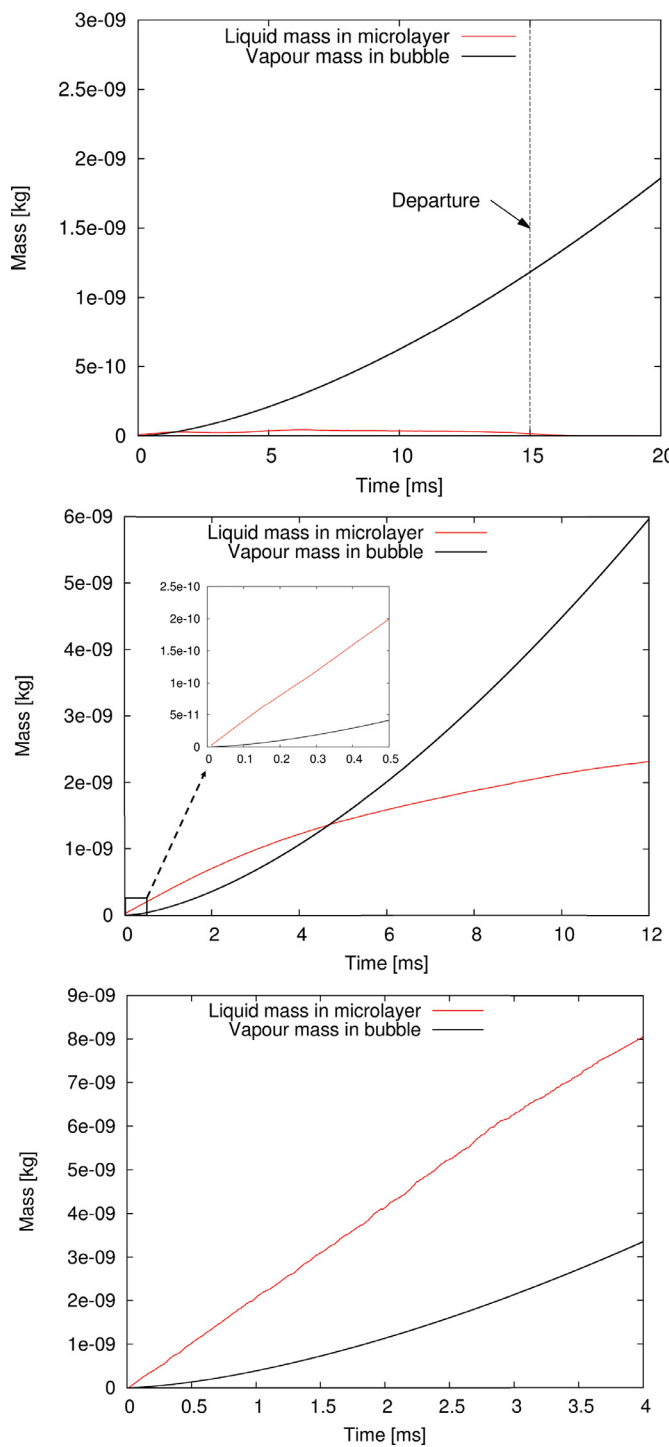


Fig. 26. Mass of liquid trapped in the microlayer compared to the vapour mass in the bubble. Top: Rate 1. Middle: Rate 2. Bottom: Rate 3.

4.1.4. Comparison of hydrodynamic-only prediction and empirical expressions

Here we compare our results against empirical correlations for the *initial* microlayer thickness. In Fig. 20 we compare our CFD hydrodynamic predictions at two times against empirical expressions for an *initial* microlayer thickness at the same bubble growth rate. It is seen that our predictions of a *hydrodynamic* microlayer thickness are generally larger than the empirical predictions for an *initial* thickness given in the literature. The fact that predicted hydrodynamic microlayer thicknesses are larger than initial thicknesses confirms the earlier observation in Figs. 6 and 19, and reinforces

Table 9

Parameters used for the simulation of the experimental case 2 (Rate 5).

Parameters	Rate 5
Growth constant β	50.19
Ja number	50.92
Simulation specifications	
Seed radius [μm]	65
Initial time [μs]	10
Initial vapour evolution rate [$\text{kg}/\text{m}^2\text{s}$]	3.95

the idea that microlayer evaporation itself must have a marked effect on the formation of microlayers.

4.1.5. Comparison of hydrodynamic-only prediction and analytical expressions

Fig. 21 compares our hydrodynamic-only predictions to analytical expressions, which are also based on pure hydrodynamic considerations. As expected our calculations agree more closely with these analytical expressions, because they do not feature the rapid evaporation of the microlayer. Our predicted thicknesses are, however, slightly smaller in close comparison.

This observed difference between our CFD calculation and the analytical models can be explained by the fact that our calculations include the effect of surface tension during microlayer formation, whilst the analytical models neglect surface tension in their analysis. The analytical models assume a perfect hemispherical shape of the bubble, whereas the bubble shape computed by the CFD tends towards an oblate caused by surface tension. This reduces the velocity with which the bubble base moves over the wall, which ultimately leads to a thinner microlayer left behind.

The presented hydrodynamic-only investigation leads us into the next section, which will incorporate the microlayer evaporation into the CFD modelling.

4.2. Validation: depletion included

We use for validation the recent experiment by Jung and Kim (2018), which succeeded in measuring microlayer profiles at very early bubble growth times. Experiments on microlayer formation during nucleate boiling were conducted in a pool of saturated water under atmospheric pressure conditions, with the properties listed in Table 4.

Extending beyond the hydrodynamic calculations above, we now include in the CFD computations the rapid evaporation from the thin microlayer formed underneath the steam bubble. This very rapid evaporation from the microlayer required a very fine near-wall mesh, with typical cell size and time steps of $0.5\ \mu\text{m}$ and $2\ \text{ns}$ respectively.

The temperature of the solid domain was initialized at a uniform superheat of 9 K , the superheat measured by the experiments. The parameters in Table 9 were selected to give the experimentally-observed growth rate, as confirmed in Fig. 22.

The predicted bubble shapes at times 0.1 ms and 0.2 ms are illustrated in Fig. 23. No bubble shape observations were available at these times to compare our results against.

In the detailed views of Fig. 23 we compare the measured microlayer thicknesses at 0.1 ms and 0.2 ms against our predictions.

As we can see our predictions of the microlayer are in reasonable agreement with the experimental data.

5. General prediction of behaviour

Encouraged by the degree of consistency seen above between predictions and measurement, we will now explore aspects of bubble behaviour predicted by the model.

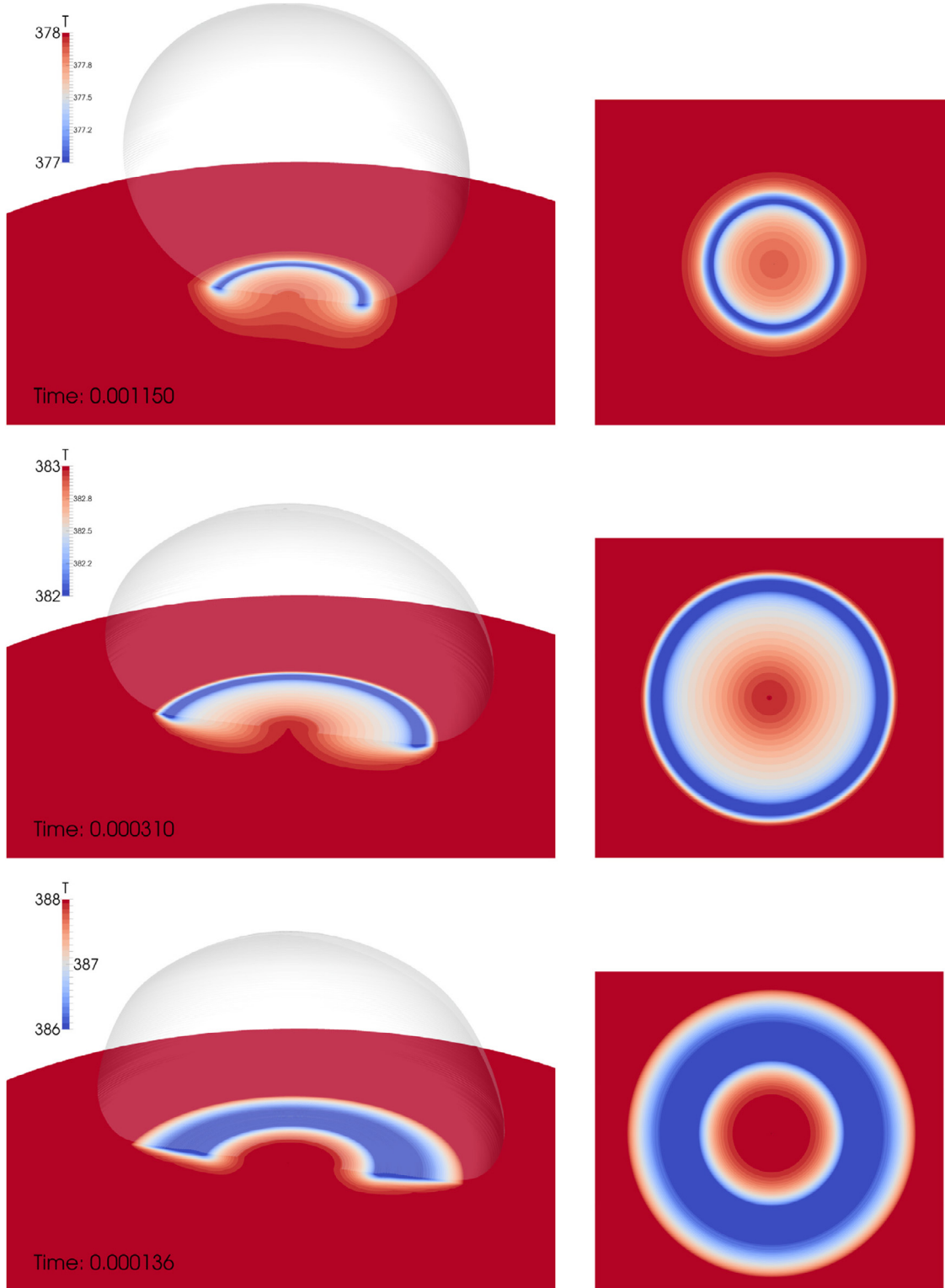


Fig. 27. CFD predictions for the three growth rates (top: Rate 1, middle: Rate 2, bottom: Rate 3). Left: Bubble shapes and temperature distributions at the same bubble equivalent diameter. Right: Top views of the wall surface temperature.

5.1. Hydrodynamic microlayer formation

We here extend the earlier hydrodynamic-only results to a full bubble life cycle, where the growth of a bubble to a typical departure diameter of $\sim 4\text{--}5\text{ mm}$ is modelled. The computational do-

main, of the general form illustrated earlier in Fig. 8, was therefore increased to $6 \times 6\text{ mm}$.

In Fig. 24 the characteristic bubble shapes, spherical for Rate 1, oblate for Rate 2 and hemispherical for Rate 3 can be identified. The detailed view of the near wall region in Fig. 25 confirms the earlier observation in Section 4.1 that there is only a contact

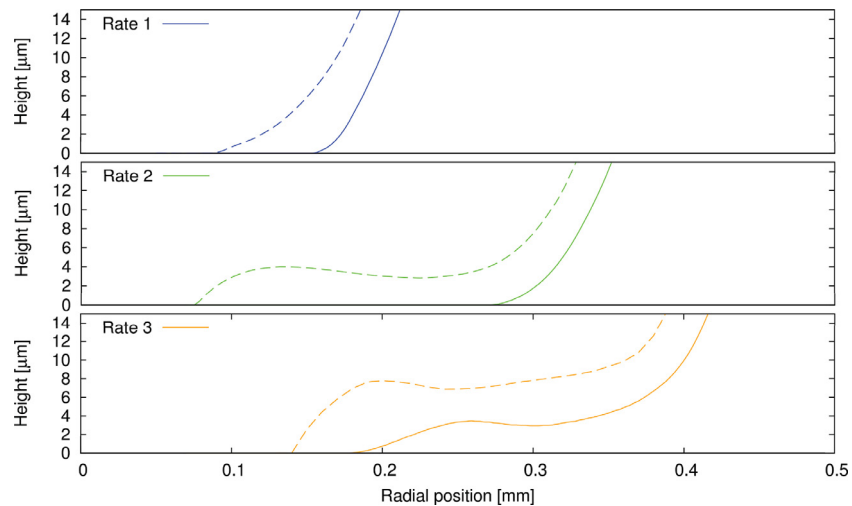


Fig. 28. Microlayer profiles for three growth rates after reaching the same bubble equivalent spherical diameter compared to the hydrodynamic-only cases (dashed lines): Rate 1 after 1.15 ms, Rate 2 after 0.31 ms and Rate 3 after 0.136 ms.

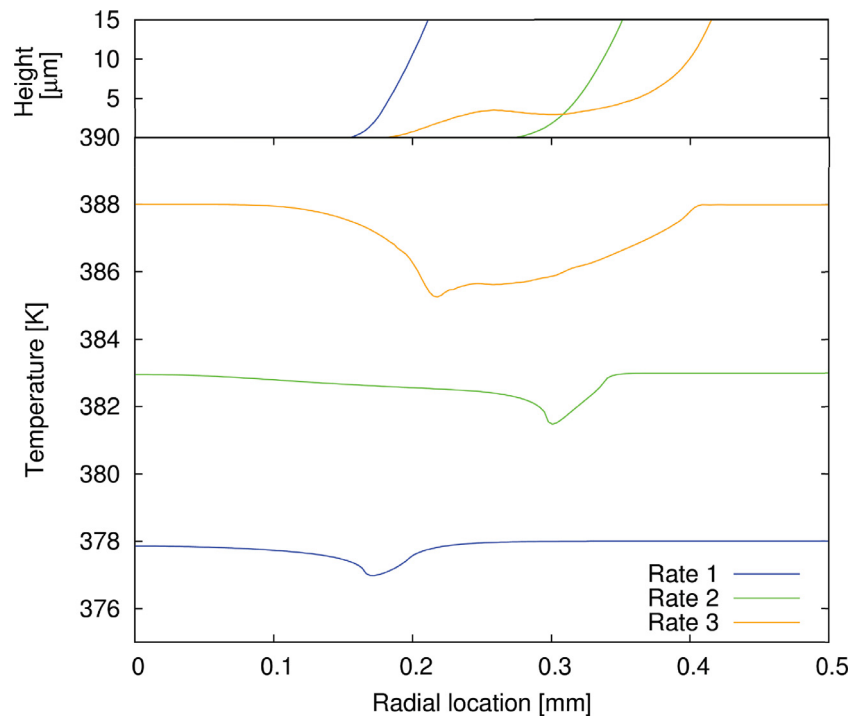


Fig. 29. Microlayer thickness (top) and wall temperature variations (bottom) for the three growth rates.

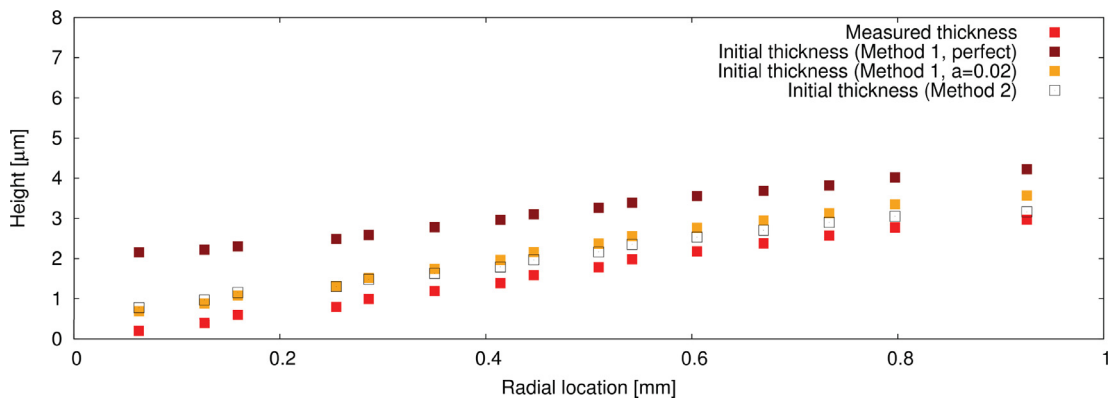


Fig. 30. Initial microlayer profiles inferred using Method 1 both incorporating and omitting evaporative thermal resistance evaporation, and the profile inferred by Method 2, compared to the measured profile.

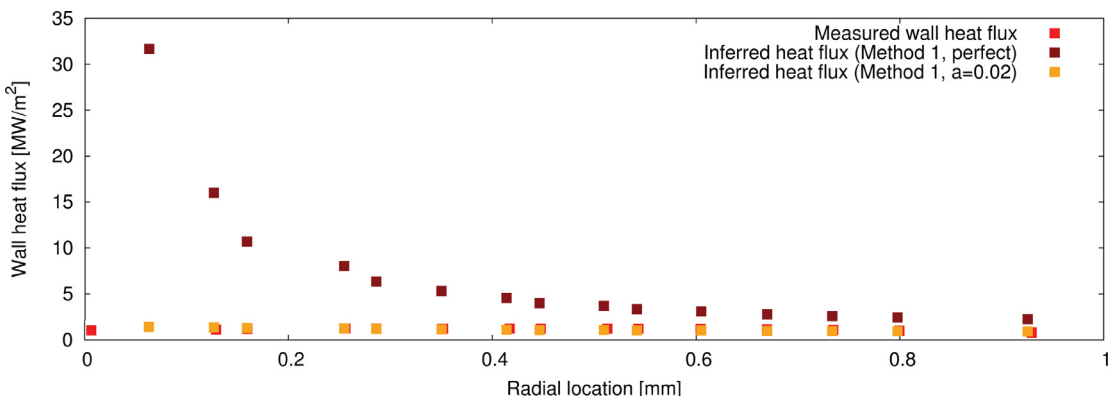


Fig. 31. Measured wall heat flux profile compared to the heat flux profiles inferred from the measured microlayer thickness by Method 1, with and without including the evaporative thermal resistance.

line for Rate 1 and a microlayer forming for Rate 2 and 3. Taken together these results provide good evidence that the microlayer formation is a consequence of the viscous flow and no-slip boundary condition at the liquid-substrate interface in the vicinity of the growing bubble.

Fig. 26 shows the liquid mass in the microlayer versus time compared to the total vapour mass inside the bubble. Subject to the comments above that the initial microlayer thickness itself is reduced by previous depletion of the microlayer at smaller radii, this comparison gives some indication of the likely contribution of vapour from the microlayer to total bubble vapour.

For Rate 1 the amount of trapped liquid is essentially zero. The small amount of liquid, still visible in Fig. 26, is caused by the tiny liquid wedge associated with the triple line, which is moving outwards until the bubble departs at ~ 15 ms.

For Rate 2 there is a substantial body of liquid trapped in the microlayer. The very early result (up to 0.5 ms), illustrated by the inset in Fig. 26, predicts that the hydrodynamic-only microlayer holds a potential vapour mass almost four times as much as is kept within the bubble. This indicates a great potential importance of microlayer evaporation during the early bubble growth stages. In the later bubble growth stages the contribution of the vapour generation from the curved surface is increasing, so that it eventually becomes the dominant vapour source after $\sim 4\text{--}5$ ms. After 12 ms, when the bubble has reached a typical departure size, the predicted hydrodynamic-only microlayer holds a vapour potential of $\sim 50\%$ of the whole bubble. The domain was still too small to allow for the departure of this bubble.

In the case of Rate 3 the mass of liquid trapped inside the microlayer remains larger than the vapour mass inside the bubble throughout the time simulated. This trapped liquid mass represents the maximum potential microlayer contribution to bubble growth for this bubble growth rate at this point.

This study suggests that the importance of microlayers, and their potential contribution to bubble growth, increases with the bubble growth rate. This corresponds to an increasing importance of microlayer evaporation with increasing wall or liquid superheat or decreasing pressure levels.

5.2. Microlayer formation and depletion

5.2.1. Low vs. high superheat bubbles

We now turn to a comparison of the predicted behaviour of low and high superheat bubbles, including the evaporation from and depletion of the microlayer. Using the characterisation above, we will denote these as 5 K, 10 K and 15 K ‘superheat’ cases. These

are the same three cases for which the hydrodynamics of microlayer formation were studied above. For each case the temperature within the solid substrate is initialized at the corresponding superheat.

Fig. 27 shows three-dimensional representations of the substrate surface temperature, at the same bubble equivalent spherical diameter, for the three different bubble growth rates. For the lower two rates the intense cooling of the solid is more or less localised at the triple line, forming a ring of reduced wall surface temperature. This is consistent with the slow growth rate tending to form little or no microlayer, with such little as does form being depleted more or less as it forms. For the more rapid growth the bubble tends towards a more hemispherical shape, as discussed above, with an associated extensive microlayer, formed rapidly. This then depletes, with an extensive, disc-shaped wall surface area thereby being cooled.

Fig. 28 plots snapshots of the predicted microlayer profiles, comparing the hydrodynamic-only case with the depleting case at each of the three applied bubble growth rates. Only for the fastest growth rate is the hydrodynamically predicted thickness large enough, and the microlayer radial growth fast enough, for an evaporating microlayer of significant extent to survive.

The corresponding temperature reductions in the substrate surface are illustrated in Fig. 29. Whereas for the two slower growth rates the temperature drop is localised at the contact line between vapour, liquid and substrate, the fastest growth rate causes a temperature reduction, which spreads radially outwards with the deepest temperature present at the inner triple line, where the microlayer is thinnest.

This is consistent with both general experimental observations and the models used to explain them. For refrigerants the vapour to liquid volume ratio is about six times smaller than water. The above modelling suggests this would lead to slower bubble growth, with then time for evaporation of the microlayer ‘as it is formed’, resulting in triple-line like behaviour. This is consistent with observations (Schweizer and Stephan, 2009; Stephan et al., 2009), and with the modelling approaches generally employed (Stephan and Hammer, 1994; Kunkelmann and Stephan, 2010) for such cases.

5.2.2. Effect of evaporative thermal resistance

We now investigate the effect of the evaporative thermal resistance on the microlayer formation and evaporation.

The need for inclusion of evaporative resistance to eliminate inconsistencies between what should otherwise be calculations of the same quantity via two different approaches was mentioned above (Section 4.1.2 (where h_{lv} is introduced)). We will investigate this here.

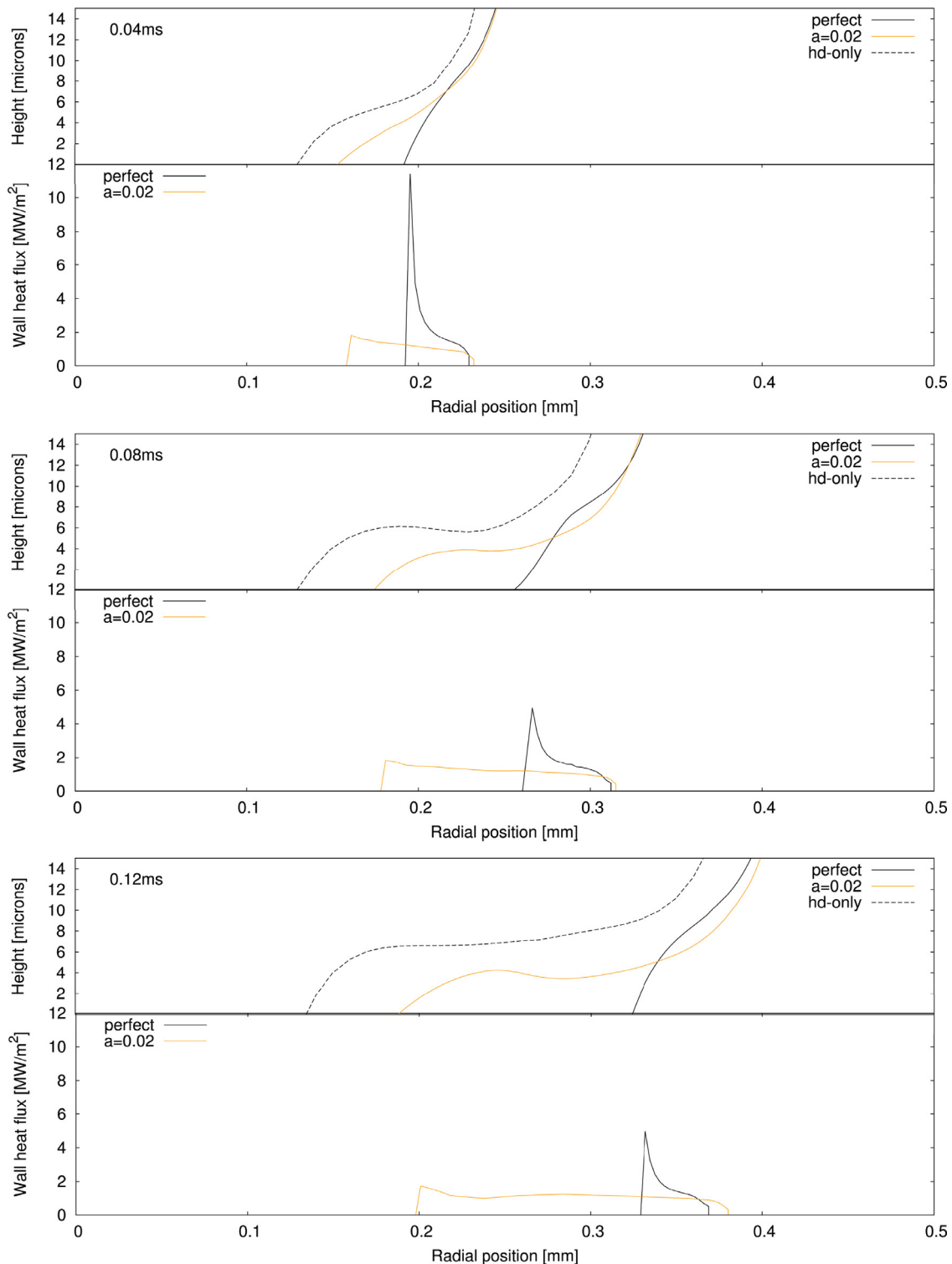


Fig. 32. Results for the fast growth rate (Rate 3) at three different times. Top: Microlayer profiles predicted for no evaporation ('hydrodynamic only') (dashed lines), 'perfect' evaporation, and case with evaporative resistance. Bottom: Associated wall heat flux profiles.

Inferring a value of evaporative resistance from experimental observations

The degree of imperfection in the evaporation process is characterized by the 'accommodation coefficient'; essentially, an indicator of the fraction of nominally-escaping vapour molecules that do not bounce back, and actually do escape the liquid. As discussed by Giustini et al. (2016), a value of the accommodation coefficient of

0.02 was suggested there to reconcile the inferred and measured microlayer thickness data of Jung and Kim (2015). This is broadly consistent with literature values of this quantity.

In Fig. 30 we show the measured initial microlayer thickness, and that inferred by the replenishment approach based only on heat removal from the substrate (Method 2 of Section 4.1.2). We also show the inferred profile based on replenishment computed

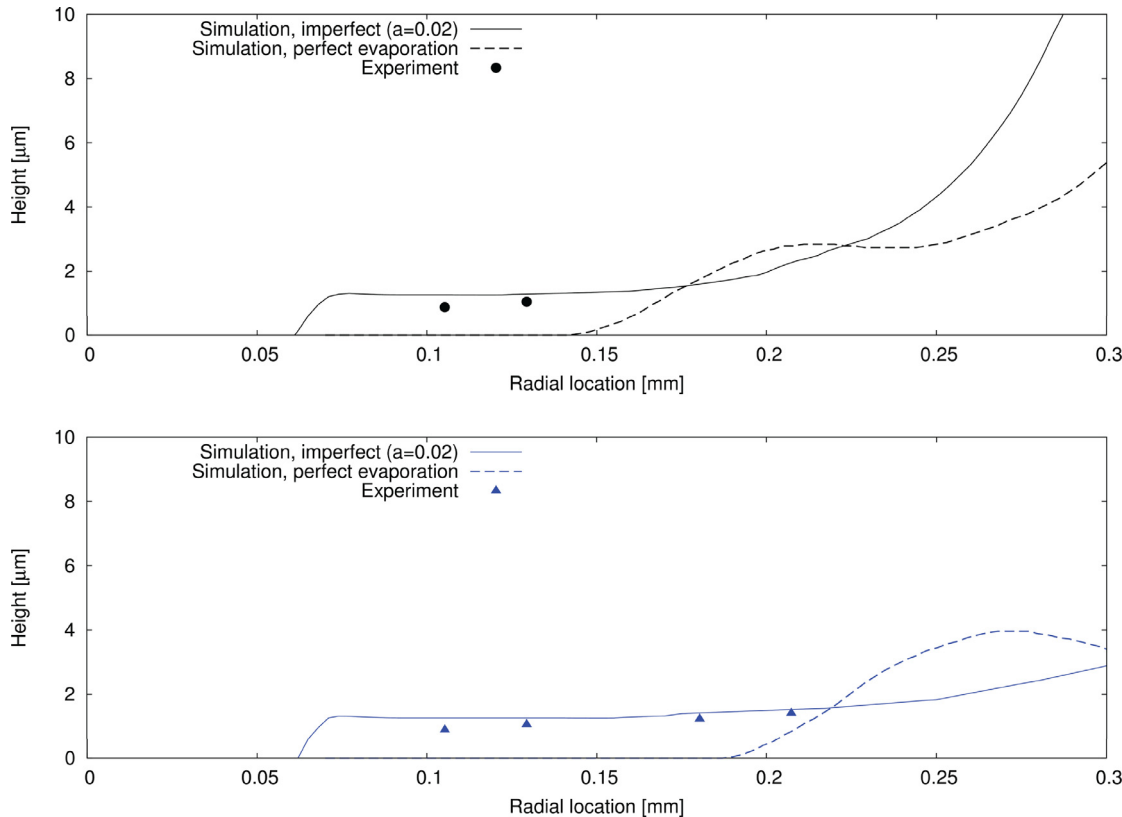


Fig. 33. Predicted microlayer profiles with and without evaporative thermal resistance compared to the measured profiles after 0.1 ms (top) and after 0.2 ms (bottom).

via conduction through the microlayer. For this latter, we use both the "best estimate" value for the evaporative resistance, and show, in addition, a case where evaporative resistance has been wholly neglected (perfect evaporation).

When assuming 'perfect' evaporation (with the interface temperature at saturation) Method 1 seems to overestimate the initial microlayer thickness. Only after including the evaporative thermal resistance, with a value of 0.02 for the accommodation coefficient, does the inferred thickness agree with the thickness inferred from the heat removal out of the solid.

Fig. 31 shows the measured wall heat flux profile compared to the conductive heat fluxes computed from the measured microlayer profiles and wall surface temperature data. When the evaporation is assumed perfect the conductive heat flux is not consistent with the measured wall heat flux profile, in particular at the inner radius of the microlayer where it is at its thinnest. When including the effect of the evaporative thermal resistance in the calculation of the conductive heat flux the predicted profile matches the measured one.

It seems that the inclusion of the effect is essential, and that a reasonable value for the coefficient here is 0.02.

The importance of incorporating evaporative resistance in predictions

We now explore the influence that evaporative resistance has on the predicted depletion of the microlayer.

We focus here on the '15K' case, where a clear microlayer has been formed, and the microlayer plays a significant role. We show in Fig. 32 microlayer profiles at three different times. These plots include the cases with no evaporation ('hydrodynamic only'), perfect evaporation, and a case with imperfection in the evaporation process.

It is seen in Fig. 32 that unimpeded, perfect evaporation essentially inhibits the prediction of the generation of a microlayer; the

microlayer is 'evaporated as soon as it is formed'. The inclusion of evaporative resistance with the accommodation coefficient of 0.02 causes a microlayer to be left behind, rather than to evaporate as quickly as it is formed. The configuration of the liquid trapped underneath the bubble base changes from a triple line to a sheet of liquid with increasing evaporative thermal resistance. It is not shown here, but in the limit as would be expected, the microlayer is predicted to tend back to the 'hydrodynamic only' form.

Also shown in Fig. 32 are corresponding predicted wall heat flux profiles. The case modelling 'perfect' evaporation predicts very high heat flux values in the range 5–12 MW/m². The heat flux magnitude is reduced and the radial extent over which it applies increases when including the evaporative thermal resistance.

We now repeat the validation case of Section 4.2, but neglecting the evaporative thermal resistance for comparison. Fig. 33 demonstrates that without the effect of the resistance the microlayer is predicted to deplete more rapidly, so that the resulting profiles no longer agree with the measurements.

In essence, the evaporative thermal resistance is seen to retard the evaporation process, allowing microlayers to be left behind and survive for a while before they are depleted. The evaporative thermal resistance thus ultimately promotes microlayer formation.

6. Conclusions

Thus far multiple experiments have observed microlayers beneath rapidly growing steam bubbles. Sophisticated measurement techniques have enabled the determination of the general configuration of these thin layers of liquid, albeit such measurements are essentially restricted to atmospheric pressures, and mostly performed for water. The finely-resolved simulations presented in this paper allow very detailed predictions to be made. Making corresponding measurements, where timescales are a few milliseconds,

and transient microlayer thicknesses are in the range of 0 to 5 µm, is very difficult. We have attempted to validate our predictions with such measurements as we can (and only recent measurements use techniques able to quantify these effects), but additional experimental data is desirable.

We have extended previous mechanistic hydrodynamic-only simulations of early microlayer formation (<1 ms). These now continue up to times of 15 ms, producing bubble diameters of ~4 mm, typical for bubble departure under atmospheric pressure. These extended computations have confirmed the understanding that the balance between inertial and surface tension forces and the resulting bubble shape determine the presence and overall extent of microlayers underneath steam bubbles. Their thickness is strongly influenced by viscous effects.

These hydrodynamic-only CFD calculations have here been augmented to include dynamic self-consistent depletion, including conjugate heat transfer into the solid substrate. Evaporation from the microlayer surface is found by computing heat transfer through the microlayer, driven by the difference between the liquid-solid interface temperature at the underside of the bubble, and the liquid-vapour interface temperature. The evaporative thermal resistance to the heat flux in the microlayer was incorporated with values for the accommodation coefficient suggested in the literature.

The microlayer depletion model is shown here to give good agreement with measured microlayers.

Noting this, the models were used to explore qualitative behaviour at high and low bubble growth rates. Predictions are that:

- For low growth rates, ~spherical bubbles are formed, with no microlayer involvement.
- For intermediate growth rates there is time for almost total microlayer depletion, causing microlayer growth more or less to be of a 'triple line' nature.
- For higher growth rates (high superheat), depletion fails to keep up with the growth of the microlayer, allowing an extensive and relatively thick microlayer to be formed, which contributes significantly to bubble growth.

Our results further suggest that the evaporative thermal resistance, by slowing down the evaporation, promotes the formation of microlayers, and that failure to include this effect can lead to quantitatively, and even qualitatively, different results. The imperfection of the evaporation process seems an important phenomenon to be considered during microlayer formation and evaporation.

Acknowledgements

The work was supported by EPSRC in collaboration with ASCOMP AG. It is a pleasure to acknowledge many helpful discussions with Raad Issa, Keith Ardron and Giovanni Giustini.

References

- ASCOMP, 2015. TransAT Handbook Series. Multiphase Flow Modelling.
- Brackbill, J.U., Kothe, D.B., Zemach Jr., C., 1992. A continuum method for modeling surface tension. *J. Comput. Phys.* 100, 335–354.
- Chen, Z., Utaka, Y., 2015. On heat transfer and evaporation characteristics in the growth process of a bubble with microlayer structure during nucleate boiling. *Int. J. Heat Mass Transfer* 81, 750–759.
- Chu, I.-C., No, H.C., Song, C.-H., 2011. A simultaneous observation of bubble growth and microlayer behaviour for an isolated boiling regime of saturated water. NURETH-14. Toronto, Ontario, Canada.
- Colombo, M., Fairweather, M., 2015. Prediction of bubble departure in forced convection boiling: A mechanistic model. *Int. J. Heat Mass Transfer* 85, 135–146.
- Cooper, M.G., Lloyd, A.J.P., 1969. The microlayer in nucleate pool boiling. *Int. J. Heat Mass Transfer* 12, 895–913.
- DasGupta, S., Schonberg, J.A., Kim, I.Y., Wayner, P.C., 1993. Use of the augmented Young-Laplace equation to model equilibrium and evaporating extended menisci. *Journal of Colloid and Interface Science* 157, 332–342.
- DasGupta, S., Kim, I.Y., Wayner Jr., P.C., 1994. Use of the Kelvin-Claeyron equation to model an evaporating curved microfilm. *J. Heat Mass Transfer* 116, 1007–1015.
- Gilman, L., Baglietto, E., 2013. Advancements on wall boiling modeling in CFD: leveraging new understanding from MIT flow boiling facility. NURETH-15. Pisa, Italy.
- Giustini, G., Jung, S., Kim, H., Walker, S., 2016. Evaporative thermal resistance and its influence on microscopic bubble growth. *Int. J. Heat Mass Transfer* 101, 733–741.
- Guion, A., 2017. Modeling and Simulation of Liquid Microlayer Formation and Evaporation in Nucleate Boiling Using Computational Fluid Dynamics. PhD Massachusetts Institute of Technology.
- Guion, A., Afkhami, S., Zaleski, S., Buongiorno, J., 2018. Simulations of microlayer formation in nucleate boiling. *Int. J. Heat Mass Transfer*.
- Hänsch, S., Narayanan, C., Reboux, S., Giustini, G., Walker, S., 2015. Microlayer models for nucleate boiling simulations: the significance of conjugate heat transfer. Nureth-16. Chicago, USA.
- Hänsch, S., Walker, S., 2016. The hydrodynamics of microlayer formation beneath vapour bubbles. *Int. J. Heat Mass Transfer* 102, 1282–1292.
- Hendricks, R.C., Sharp, R.R., 1964. Initiation of Cooling due to Bubble Growth on a Heating Surface. NASA.
- Johnson, M.A., Javier De La Peña, J., Mesler, R.B., 1966. Bubble shapes in nucleate boiling. *AIChE J.* 12, 344–348.
- Jung, S., Kim, H., 2014. An experimental method to simultaneously measure the dynamics and heat transfer associated with a single bubble during nucleate boiling on a horizontal surface. *Int. J. Heat Mass Transfer* 73, 365–375.
- Jung, S., Kim, H., 2015. An experimental study on heat transfer mechanisms in the microlayer using integrated total reflection, laser interferometry and infrared thermometry technique. *Heat Transfer Eng.* 36, 1002–1012.
- Jung, S., Kim, H., 2018. Hydrodynamic formation of a microlayer underneath a boiling bubble. *Int. J. Heat Mass Transfer* 120, 1229–1240.
- Kim, H., Buongiorno, J., 2011. Detection of liquid-vapor-solid triple contact line in two-phase heat transfer phenomena using high-speed infrared thermometry. *Int. J. Multiphase Flow* 37, 166–172.
- Koffmann, L.D., 1980. I. Experimental Observations of the Microlayer in Vapor Bubble Growth on a Heated Solid. II. An investigation of the Theory of Evaporation and Condensation. PhD California Institute of Technology.
- Koffmann, L.D., Plesset, M.S., 1983. Experimental observations of the microlayer in vapor bubble growth on a heated solid. *J. Heat Transfer* 105, 625–632.
- Kunkelmann, C., Stephan, P., 2010. Numerical simulation of the transient heat transfer during nucleate boiling of refrigerant HFE-7100. *Int. J. Refrig.* 33, 1221–1228.
- Mitrovic, J., 1997. Formation of a liquid jet after detachment of a vapour bubble. *Int. J. Heat Mass Transfer* 40, 4309–4317.
- Moore, F.D., Mesler, R.B., 1961. The measurement of rapid surface temperature fluctuations during nucleate boiling of water. *AIChE J.* 7, 620–624.
- Olander, R.R., Watts, R.G., 1969. An analytical expression of microlayer thickness in nucleate boiling. *J. Heat Transfer* 91, 178–180.
- Phan, H.T., Caney, N., Marty, P., Colasson, S., Gavillet, J., 2009. How does surface wettability influence nucleate boiling? *C. R. Mecanique* 337, 251–259.
- Sakashita, H., 2011. Bubble growth rates and nucleation site densities in saturated pool boiling of water at high pressures. *J. Nucl. Sci. Technol.* 48, 734–743.
- Sato, Y., Ničeno, B., 2015. A depletable micro-layer model for nucleate pool boiling. *J. Comput. Phys.* 300, 20–52.
- Schrage, R.W., 1953. A Theoretical Study of Interphase Mass Transfer. Columbia University Press, New York.
- Schweizer, N., Stephan, P., 2009. Experimental study of bubble behavior and local heat flux in pool boiling under variable gravitational conditions. *Multiphase Sci. Technol.* 21, 329–350.
- Scriven, L.E., 1959. On the dynamics of phase growth. *Chem. Eng. Sci.* 10, 1–13.
- Smirnov, G.F., 1975. Calculation of the initial thickness of the microlayer during bubble boiling. *J. Eng. Phys.* 28, 369–374.
- Stephan, P., Fuchs, T., Wagner, E., Schweizer, N., 2009. Transient Local Heat Fluxes during the entire vapor bubble life time. ECI International Conference on Boiling Heat Transfer.
- Stephan, P., Hammer, J., 1994. A new model for nucleate boiling heat transfer. *Wärme- und Stoffübertragung* 30, 119–125.
- Sussmann, M., Smereka, P., Osher, S., 1994. A level set approach for computing solutions to incompressible two-phase flow. *J. Comput. Phys.* 114, 146–159.
- Urbano, A., Tanguy, S., Huber, G., Colin, C., 2018. Direct numerical simulation of nucleate boiling in micro-layer regime. *Int. J. Heat Mass Transfer* 123, 1128–1137.
- Utaka, Y., Kashiwabara, Y., Ozaki, M., 2013. Microlayer structure in nucleate boiling of water and ethanol at atmospheric pressure. *Int. J. Heat Mass Transfer* 57, 222–230.
- Utaka, Y., Kashiwabara, Y., Ozaki, M., Chen, Z., 2014. Heat transfer characteristics based on microlayer structure in nucleate pool boiling for water and ethanol. *Int. J. Heat Mass Transfer* 68, 479–488.
- Van ouwerkerk, H.J., 1971. The rapid growth of a vapour bubble at a liquid-solid interface. *Int. J. Heat Mass Transfer* 14, 1415–1431.
- Van stralen, S.J.D., Sohal, M.S., Cole, R., Slyuter, W.M., 1975. Bubble growth rates in pure and binary systems: Combined effect of relaxation and evaporation microlayers. *Int. J. Heat Mass Transfer* 18, 453–467.
- Yabuki, T., Nakabeppu, O., 2014. Heat transfer mechanisms in isolated bubble boiling of water observed with MEMS sensor. *Int. J. Heat Mass Transfer* 76, 286–297.
- Yabuki, T., Saitoh, T., Nakabeppu, O., 2013. Contribution of microlayer evaporation to bubble growth in pool saturated boiling of water. ASME 2013 11th International Conference on Nanochannels, Microchannels, and Minichannels.